Studying half-Heusler based materials for thermoelectric application

A Thesis

submitted to
Indian Institute of Science Education and Research Pune
in partial fulfillment of the requirements for the
BS-MS Dual Degree Programme

by

Nupur Sontakkey

Indian Institute of Science Education and Research Pune
Dr. Homi Bhabha Road,
Pashan, Pune 411008, INDIA.

April, 2020

Supervisor: Dr. Surjeet Singh
© Nupur Sontakkey 2020

All rights reserved

Certificate

This is to certify that this dissertation entitled Studying half-Heusler based materials for thermoelectric applicationtowards the partial fulfilment of the BS-MS dual degree programme at the Indian Institute of Science Education and Research, Pune represents study/work carried out by Nupur Sontakkey at Indian Institute of Science Education and Research under the supervision of Dr. Surjeet Singh, Associate Professor, Department of Physics , during the academic year 2019-2020.

12.4.20

Dr. Surjeet Singh

सुरजीत सिहँ / Surjeet Singh
सहयोगी प्राध्यापक / Associate Professor
भारतीय विज्ञान शिक्षा एवं अनुसंधान संस्थान
Indian Institute of Science Education & Research
पुणे / Pune - 411 008, India

Committee:

Dr. Surjeet Singh

Prof. Satishchandra Ogale

This thesis is dedicated to my parents and my sister, Sana.
This would'nt have been possible without you guys!

Declaration

I hereby declare that the matter embodied in the report entitled Studying half-Heusler based materials for thermoelectric application are the results of the work carried out by me at the Department of Physics, Indian Institute of Science Education and Research, Pune, under the supervision of Dr. Surjeet Singh and the same has not been submitted elsewhere for any other degree.

12.4.20

सुरजीत सिहँ / Surjeet Singh
सहयोगी प्राध्यापक / Associate Professor
भारतीय विज्ञान शिक्षा एवं अनुसंधान संस्थान
Indian Institute of Science Education & Research
पुणे / Pune - 411 008, India

Nupur Sontakkey

Acknowledgments

I would like to thank my supervisor, Dr. Surjeet Singh, for allowing me to work on this project and for his keen interest and valuable guidance whenever I was stuck during the project. Even during his busy schedule, he was always willing to help. His valuable suggestions, comments and ideas have helped shape this thesis.

I would also like to thank my labmates, Luminita Ma'am, Dr.Rabindra Bag, Prachi, Saurabh, Dibyata, Navita, Anupam, Haritha, Prakash, Sanchyeta, Pragna, Ankit, Nashra and Sagar for making the lab environment ideal for work. Their timely support and encouragement have helped me at various stages of my work. The weekly Thermoelectric group meetings were immensely helpful in impacting my understanding of the topic and improving my presentation skills. I would especially like to thank Saurabh Bhaiya for helping me with the necessary techniques required, his unending support and motivation.

I would like to thank my friends Bhawana, Heena, Rani, Roshni, and Swati for putting up with my craziness, motivating, and supporting me all the time. Most importantly making this five years journey such an awesome one. I would also like to thank my Tamil mess group Aswani, Athunya, and Kiran.

You people were a beautiful family away from home.

I wish to express my gratitude towards h-cross technical staff Mr. Anil, Mr. Nilesh, Mr. Sudhir, Mr. Yatish, who played an essential part in this thesis work. I would also like to thank the Government of India for the INSPIRE scholarship during the BSMS course.

Last but not least, the people who have always been a source of inspiration to me, I wish to thank Mummy, Papa, and Sana for always being there.

Abstract

Since the fossil fuels are limited, and are fast depleting, there is an urgent need to search for alternative energy sources that are, both, clean and economically viable. Thermoelectric (TE) devices can play a crucial role in this direction as they have the potential to convert "waste heat" into electricity. Here, the term "waste heat" refers to the heat which is generated by, the exhaust of an industrial chimney or an automobile, or even the microprocessor chip of a laptop. Tapping waste heat and converting it into useful energy using TE devices is a seemingly good idea; however, its widespread use is limited by the low efficiency of the current TE devices, which makes the energy production cost economically unviable. To come out of this conundrum it is therefore necessary to search for new TE materials to improve the conversion efficiency.

In this work, we investigate the half-Heusler (HH) compounds TaCoSn and NbFeSb for their potential as p-type thermoelectrics. Using theoretical calculations it was shown that TaCoSn should crystallize in a HH structure with superior TE properties. However, as of today, there are no reports on the single phase synthesis of TaCoSn. We studied the possibility of HH phase formation in TaCoSn using the solid state reaction route under various synthesis conditions.

On the other hand, NbFeSb is known to crystallize with the HH structure. It also shows promising TE properties, which we plan to improve further by doping at the Fe site which has not been explored that well. The sign of thermopower of undoped NbFeSb shows a sample dependence. We have, therefore, investigated the effect of Nb off- stoichiometry on the thermopower and TE properties. In a bid to increase the TE performance, we also investigated the effect of Ru doping in $Nb_{0.86}Hf_{0.14}FeSb$. The highest TE figure of merit (ZT) of 0.88 near 900K.

Contents

Abstract **xi**

1 Introduction **1**

2 Experimental Techniques **9**

2.1 Arc Melting 9

2.2 Material Synthesis 10

2.3 X-ray Diffraction 15

2.4 FESEM 17

2.5 Seebeck and Electrical Resistivity measuring unit 18

2.6 Laser Flash Analyzer (LFA) 19

3 Results and Discussions **23**

3.1 XRD 23

3.2 FESEM 30

3.3 TE Measurements: Thermopower, Electrical conductivity and PF 35

3.4 TE Measurements: Thermal conductivity and ZT for doped NbFeSb samples 43

4 Conclusion **47**

List of Figures

1.1 Thermoelectric Effects 2

1.2 Relation between the thermoelectric parameters 3

1.3 Phonon scattering Mechanisms 5

1.4 Half Heusler structure 6

2.1 Arc melting Furnace 10

2.2 Temperature profile for TaCoSn 11

2.3 X-ray Diffraction fig (a) show the braggs law where θ is the incident angle, d is the distance between the plane, fig(b) is the image of the instrument . . . 16

2.4 Field Emission scanning electron microscope (a) show comparision of FESEM and Light microscope, fig(b) is the image of the instrument 17

2.5 Schematics of measurement setup for measuring thermopower and electrical resistivity 18

2.6 LFA instrument 21

3.1 XRD pattern of TaCoSn samples 25

3.2 XRD comparison of all TaCoSn samples; black: simulated, red: Sintering-1 TaCoSn_01, blue: Sintering-2 TaCoSn_02, pink: Sintering-1 TaCoSn_03, green: Sintering-1 TaCoSn_04 26

3.3 XRD pattern for pristine NbFeSb samples; (a) NbFeSb_01_03, (b) NbFeSb_02_02 27

3.4 XRD pattern for Nb off-stoichiometric NbFeSb samples; 28

3.5 XRD pattern for Ru doping at Fe site in NbFeSb 28

3.6 XRD pattern for Ru doping at Fe site in $Nb_{0.86}Hf_{0.14}FeSb$ 29

3.7 FESEM images of NbFeSb pristine samples 30

3.8 FESEM image of off stoichiometric samples 31

3.9 FESEM image of Ru doping at Fe site in NbFeSb samples 32

3.10 FESEM images of Ru doping at Fe site in $Nb_{0.86}Hf_{0.14}FeSb$ 33

3.11 FESEM Stoichiometric analysis of all NbFeSb samples; Here nfsr3 is for $NbFe_{0.97}Ru_{0.03}Sb$, nfsr5 is $NbFe_{0.95}Ru_{0.05}Sb$, nfshr3 is for $Nb_{0.86}Hf_{0.14}Fe_{0.97}Ru_{0.03}Sb$ and nfshr5 is for $Nb_{0.86}Hf_{0.14}Fe_{0.95}Ru_{0.05}Sb$ 34

3.12 LSR measurements of TaCoSn 03 36

3.13 TE measurements of NbFeSb samples; (a), (b), and (c) are Thermopower, Electrical conductivity, and PF respectively for NbFeSb_02_02 sample and (d) is Thermopower of NbFeSb_01_03 sample. Here, reported values refers to ref. [20] reports of TE measurement, and AM refers to ref. [1] work 37

3.14 TE measurements of $Nb_{1+x}FeSb$ samples (a) Seebeck Coefficient, (b) Electrical conductivity, (c) Power Factor; Here, n1.3fs refers to the Nb excess sample $Nb_{1.3}FeSb$ [x=0.3], N0.95FS is $Nb_{0.95}FeSb$[x=-0.05], N0.769FS is $Nb_{0.769}FeSb$ [x=-0.23], while NFS0103 and NFS0202 are the pristine sample NbFeSb_01_03 and NbFeSb_02_02 [x=0] respectively and reported refers to ref. [20] reports of negative S 39

3.15 TE measurements of Ru doped samples (a) Thermopower, (b) Conductivity, and (c) PF ; Here, nfsr3 is for $NbFe_{0.97}Ru_{0.03}Sb$, nfsr5 is $NbFe_{0.95}Ru_{0.05}Sb$, nfs0202 is NbFeSb_02_02 and 'h' stands for heating data while 'c' for cooling data 41

3.16 TE measurements for Ru doping at Fe site in $Nb_{0.86}Hf_{0.14}FeSb$ samples (a) Thermopower measurement, (b) Conductivity and (c) PF; Here, nfshr3 is for $Nb_{0.86}Hf_{0.14}Fe_{0.97}Ru_{0.03}Sb$, nfshr5 is for $Nb_{0.86}Hf_{0.14}Fe_{0.95}Ru_{0.05}Sb$ 42

3.17 Thermal conductivity of all doped NbFeSb samples; Here nfsr3 is for $NbFe_{0.97}Ru_{0.03}Sb$, nfsr5 is $NbFe_{0.95}Ru_{0.05}Sb$, nfsh is for $Nb_{0.86}Hf_{0.14}FeSb$, nfshr3 is for $Nb_{0.86}Hf_{0.14}Fe_{0.97}Ru_{0.03}Sb$ and nfshr5 is for $Nb_{0.86}Hf_{0.14}Fe_{0.95}Ru_{0.05}Sb$, NFSH0.15_AM is reported data for $Nb_{0.85}Hf_{0.15}FeSb$ by Tavassoli *et.al.*[1], NFSH_0.14_AM_2 is reported data for $Nb_{0.86}Hf_{0.14}FeSb$ by Fu *et.al.*[2] 44

3.18 ZT of doped NbFeSb samples; (a) ZT for Ru doping at Fe site in NbFeSb (b) ZT for Ru doping at Fe site in $Nb_{0.86}Hf_{0.14}FeSb$ samples. Here, nfsr3 is for $NbFe_{0.97}Ru_{0.03}Sb$, nfsr5 is $NbFe_{0.95}Ru_{0.05}Sb$,nfshr3 is for $Nb_{0.86}Hf_{0.14}Fe_{0.97}Ru_{0.03}Sb$ and nfshr5 is for $Nb_{0.86}Hf_{0.14}Fe_{0.95}Ru_{0.05}Sb$.While, 'h' stands for heating data and 'c' for cooling data. 45

List of Tables

2.1 Pristine NbFeSb Sample preparation Summary 13

2.2 Sample preparation Summary 15

3.1 lattice parameter 29

3.2 Summary of impurity phases in various samples as detected using Powder X-ray diffraction and FESEM techniques 34

Chapter 1

Introduction

Thermoelectric (TE) materials convert heat to electricity and vice versa based on the Seebeck and Peltier effect. TE devices find applications in heating and cooling as well as energy harvesting. Different TE materials have application in different temperature ranges. For example, near the room temperature region (300–500K), traditional $(Bi, Sb)_2(Te, Se)_3$ based TE materials can be used. For moderate temperature range (500–900K), PbTe, SnTe, and skutterudites are useful TE materials; and finally, in the high-temperature region ($\geq$ 900 K), SiGe alloy has been promising. Recently, a class of compounds known as half-Heuslers have been identified as an excellent thermoelectric material for the high-temperature region, and are therefore potential candidate materials for waste heat management in industrial plants and for other high temperature applications.

In the subsequent sections, we will introduce various TE effects, and define the TE figure of merit of material, which characterizes the goodness of a material as a potential TE. We will then introduce the half-Heusler (HH) structure, which will be followed by a brief survey of previous TE studies done on these materials.

1.0.1 Thermoelectric Effects

Thermoelectric effect was first observed by T.J. Seebeck in 1821 termed as Seebeck effect. In the year 1834, J. Peltier discovered the second thermoelectric effect known as the Peltier effect.[11]

SEEBECK EFFECT: Temperature difference at the junction of two dissimilar metals leads to a current flow in the circuit. This conversion of a temperature difference to electricity is known as the Seebeck effect.The Seebeck coefficient is given by: S= ΔV/T where, ΔV is the voltage generated (in V) and T is the temperature gradient applied (in K).

PELTIER EFFECT: Peltier effect is an inverse of the Seebeck effect. Current flow through the circuit made of two dissimilar metals/conductors leads to temperature difference at their junctions. The peltier Coefficient is given by: π = Q/I where, Q is the rate of heating or cooling (in J/s)and I is the current passed (in A).

Figure 1.1(a) shows a device working on the principle of Seebeck effects. In this figure, N and P denotes n-type and p-type semiconductors respectively. Their junctions are connected to a heat source and heat sink creating a temperature difference between the junction. The carriers at the hot end gain energy and diffuse towards the cold end. This movement of carriers leads to a flow of current through the entire circuit as shown in the figure.
While in the fig 1.1(b), instead of creating a temperature difference at the junctions, voltage difference has been created. This leads to absorbtion of heat at the junction connected to higher voltage, and the other junction is cooled, which is the principle on which the Peltier coolers work.

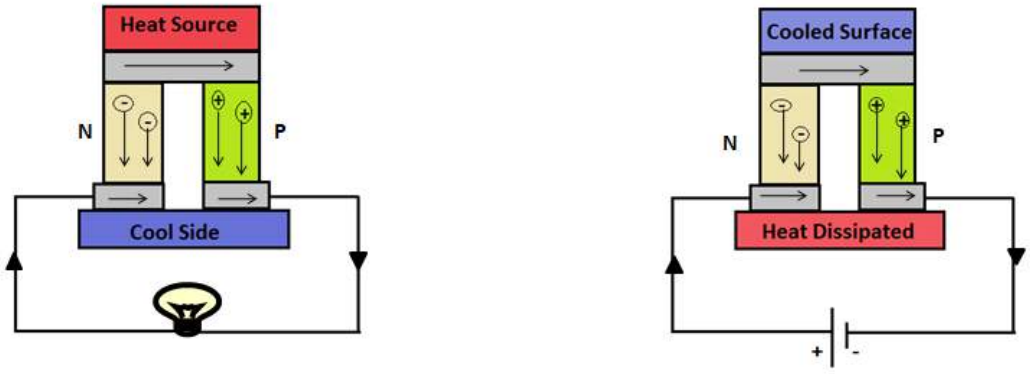

(a) Seebeck effect (b) Peltier effect

Figure 1.1: Thermoelectric Effects

Thermoelectric devices convert heat to electricity and vice versa without any emission or moving part. However, one of the drawbacks of TE devices is their low conversion efficiency, which makes them economically inviable.
The efficiency of a thermoelectric device is defined as:

$$\eta = (\frac{T_{hot} - T_{cold}}{T_{hot}}) * \frac{\sqrt{1 + ZT_{avg}} - 1}{\sqrt{1 + ZT_{avg}} + \frac{T_{cold}}{T_{hot}}} \tag{1.1}$$

where, T_{hot} is the hot side temperature, T_{cold} is the cold side temperature, ZT_{avg} is the average dimensionless figure of merit. η is dependent on $(\frac{T_{hot}-T_{cold}}{T_{hot}})$, the Carnot efficiency of a device, and the figure of merit (ZT) which is a materials property. The figure of merit ZT is a dimensionless quantity given by:

$$ZT = \frac{S^2 T \sigma}{(\kappa_e + \kappa_l)} \tag{1.2}$$

$$S = \frac{8\pi^2 k_B^2}{3eh^2} m_d^* T (\frac{\pi}{3n})^{\frac{2}{3}} \tag{1.3}$$

$$\sigma = ne\mu \tag{1.4}$$

Here, S is the Seebeck coefficient, σ the electrical conductivity, μ is the carrier mobility, n is carrier concentration, m_d^* is density of states effective mass, and κ the total thermal conductivity, which consists of electrical thermal conductivity (κ_e) and lattice thermal conductivity(κ_l).

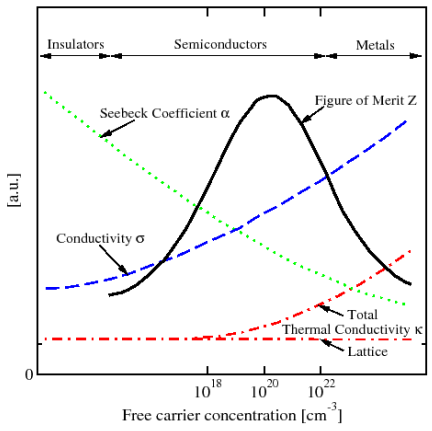

Figure 1.2: Relation between the thermoelectric parameters

The ZT of material therefore depends on the parameters S, σ, and κ. As seen in the fig 1.2, S and σ are related to the carrier concentration (n). If n increases σ increases but S decreases (this relation is also evident from the equation 1.3 and 1.4), and since κ_e and σ are related via the Wiedemann–Franz law, κ_e also increases with increase in σ. So, improving one parameter deteriorates the other. Hence, decoupling these parameters is not very easy and is an active area of research for different classes of TE materials.

Various strategies have been applied for improving ZT. Doping and alloying is used to alter the band structure and enhance the thermoelectric performance of a materials. Mahan and Sofo proposed that TE performance can be improved if electrons in a narrow distribtion of energy participate in transport.[13] This, in turn, can be realized by what is known as the resonant doping, which was experimentally realized for the first time by Heremans *et.al.* in PbTe via Tl doping[12]. Later resonant dopants were reported for many different materials like tin for Bi_2Te_3 valance band (VB) [15], indium for SnTe VB [16], aluminum in PbSe conduction band[14].

Thermoelectric properties can also be improved by band convergance. From equation 1.3, we see that $S \propto m_d^*$ the density of state effective mass (m_d^*) and $\mu \propto (1/m_b^*)$ the band effective mass (m_b^*). While m_d^* and m_b^* are related to each other via band degeneracy (N_V): $m_d^* = N_V{}^{2/3}\, m_b^*$. Hence, enhancement in density of states effective mass can be achieved by improving the band degeneracy. Band degenaracy in turn increases when multiple bands have their band extrema with negligible energy difference. Increasing the band degeneracy (N_V) is an effective strategy to enhance Seebeck coefficient without compromising the mobility.

Doping may also optimize the carrier concentration, as n is the main coupling factor for TE parameters, and hence can be used as an effective way of increasing the power factor (PF), which is simply the square of thermopower times the electrical conductivity. It is known that the thermal conductivity of a material is dependent on both k_l and k_e. However, the lattice thermal conductivity is independent of other TE parameters, hence, it is sometimes useful to reduce k_l by a phonon scattering mechanisms, for example, like phonon-phonon scattering, umklapp scattering, acoustic and optical phonon scattering, anharmonicity, hierarchical phonon scattering etc. (fig 1.3)

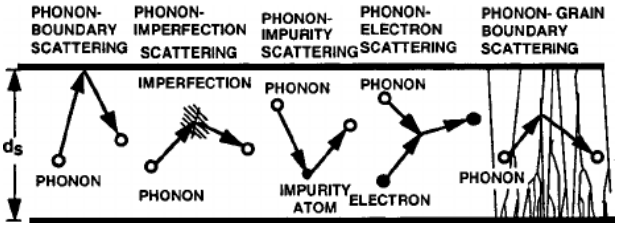

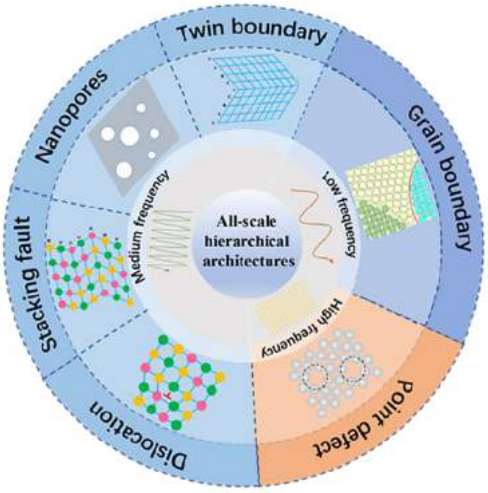

Figure 1.3: Phonon scattering Mechanisms
[18][19]

1.0.2 Half-Heusler alloys as potential TEs

Half-Heusler have intrinsically high PF [6] and have been extensively studied for thermoelectric applications. They are ternary intermetallics, with formula XYZ (space group = 216, F-43M); where, XY- forms NaCl type structure, YZ- forms ZnS type structure; where X- late TM (Transition Metal), Y- early TM, and Z- p block element. Despite being intermetallics, some of these are found to be semiconducting. This family of compounds are also studied for their piezoelectric, superconductivity, ferroelectric, topological, and other interesting properties.

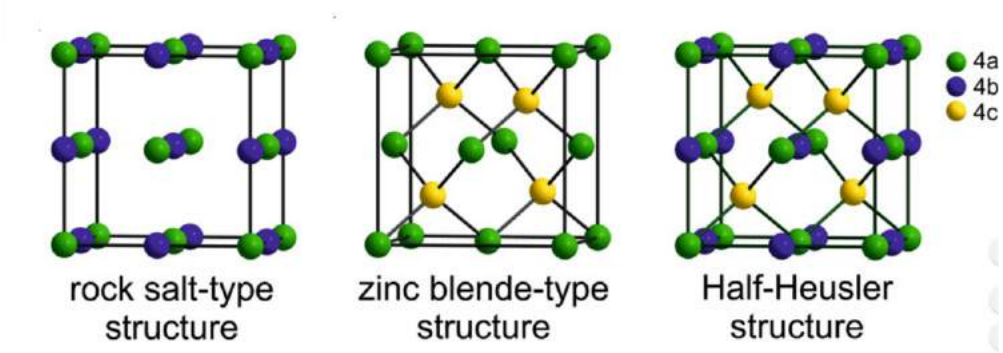

Figure 1.4: Half Heusler structure
[10]

In this work, we will focus on the half-Heuslers compounds TaCoSn and NbFeSb.

There have been very few reports on TaCoSn[7][8][9]. Recently, Zakutayev *et al.* experimentally realized TaCoSn in the HH structure but with several secondary phases, including Co_2Ta, CoSn, and $CoSn_2$. They argued that it could be due to surface oxidation of Ta powder kinetically limiting the reaction process[9]. Here, we carried out experiments to synthesize TaCoSn using solid state reaction route starting from powders of Ta, Co and Sn, and by sealing them in evacuated quartz ampoules and subjecting them to varied heat treatments.

MFeSb (M=V, Nb, Ta) compounds were earlier studied as n-type thermoelectrics, and the highest ZT of 0.33 (VFeSb) was achieved. It was later realized that VFeSb has a similar band structure as a p-type HH (ZrCoSb) and also $N_v = 8$ for valance band maximum while $N_v = 3$ for conduction band minimum. Further study on VFeSb led to the realization of p-type NbFeSb. Currently, NbFeSb is considered as a promising p-type thermoelectric material[4]. Being degenerate semiconductors, with carrier concentration ranging from 10^{18} to 10^{19} per cm^3, these HH compounds exhibit high electrical conductivity, but thanks to the high valley degeneracies associated with their valance and conduction bands, they also exhibit a high thermopower and hence a reasonably high power factor. But the downside of having a high electrical conductivity is that the thermal conductivity of these materials is also often very high, which does not allow ZT to take high enough values. Thus, one of the ways to increase ZT is to reduce the lattice thermal conductivity without adversely affecting the power factor.

Fu *et.al.* showed that Hf being a heavier dopant can decouple the thermoelectric parameters in heavy band half Heusler compound NbFeSb[2]. Hf results in more point defect

scattering and is more efficient in supplying carriers as compared to Zr and Ti. Hence, κ_l and PF are improved significantly as compared to Ti or Zr doping [2]. Further, Ru doping at the Fe site may lead to mass fluctuation and reduce thermal conductivity. Hence, in this work we have tried to study the effect of Ru doping at Fe site in $Nb_{0.86}Hf_{0.14}FeSb$ and NbFeSb.

Chapter 2

Experimental Techniques

2.1 Arc Melting

In this chapter we will discuss various experimental techniques that have been employed during the course of this work. We will start by describing the working principle of an arc-melter, which was used extensively during the course of this thesis for sample synthesis

Arc Melting furnace is generally used for synthesis of inter-metallic alloys and compounds. The furnace consists of a water cooled copper hearth and a replaceable tungsten electrode. The hearth configuration is such that it can accommodate three samples and a Zr getter. The chamber is purged five times and finally filled with argon for inert atmosphere to avoid oxidation of the sample during melting. Then, a high voltage current is passed through the electrode, which produces an arc that provides energy for melting. The Zirconium getter is melted before the sample. The sample is flipped three to four times to ensure homogeneity.

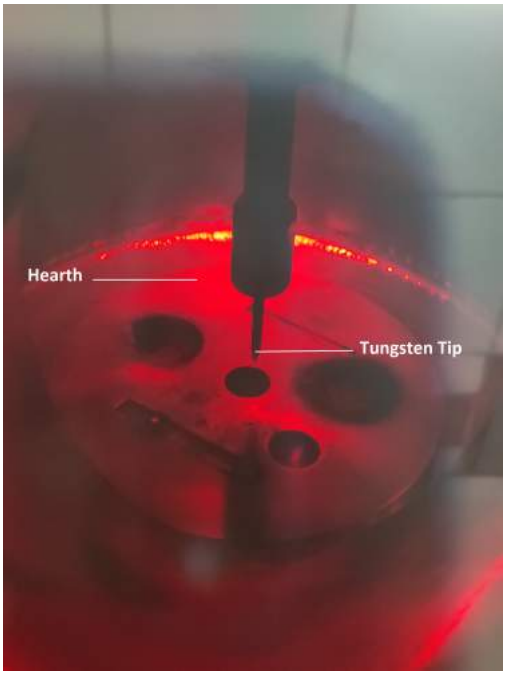

(a) Water cooled copper hearth and the tungsten filament

(b) Arc melting Furnace

Figure 2.1: Arc melting Furnace

2.2 Material Synthesis

2.2.1 TaCoSn

During the course of our investigations we carried out four different synthesis experiments to realize single phase TaCoSn. The details of the the synthesis and the results obtained are describribed below.

• TaCoSn_01: The starting materials were Ta, CO, and Sn. These were taken in the form of high purity powders ($>$ 99.9% purity precursors purchased from Alfa Aesar and Sigma Aldrich). The precursors were weighed and mixed for 1 hr inside an argon filled glove box with O_2 and moisture level always maintained at $<$ 1 ppm. The well mixed powders were taken out and immediatly pelletized to reduce exposure to the air. The pellets were sealed in an evacuated quartz tube and kept for sintering at 600^{o}C. The sintered pellets were grinded,

pelletized and sealed again for second sintering at 1000^{o}C. (Temperature profile is shown in figure 2.2)

• TaCoSn_02: The precursors were weighed, mixed and pelletized as described above. The pellets were sealed in a quartz tube and kept for sintering at 600^{o}C. The sintered pellets were ground, pelletized and sealed again for second sintering at 600^{o}C. (Temperature profile is shown in figure 2.2)

• TaCoSn_03: The precursors were weighed, mixed and pelletized as described above. The pellets were sealed in a quartz tube and kept for sintering at 600^{o}C. (Temperature profile is shown in figure 2.2)

• TaCoSn_04: The precursors were weighed and transferred to the ampoule inside the glove box without pelletizing. The argon filled ampoule was taken out of the glove box with a stop-cock to prevent air from replacing the Ar gas inside. It was then evacuated and sealed immediately. It was further sintered at 600^{o}C. (Temperature profile is shown in figure 2.2)

Sr. No.	Sample	Temperature Profie 1st sintering	Temperature Profile 2nd sintering
1	TaCoSn_01 (SM72)	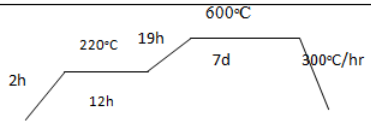	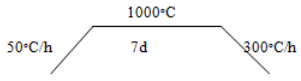
2	TaCoSn_02 (SM73)	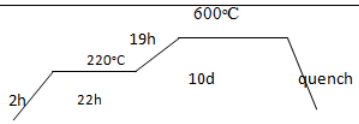	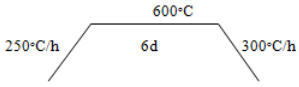
3	TaCoSn_03 (SM74)	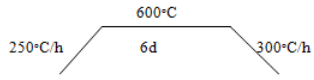	
4	TaCoSn_04 (SM75)	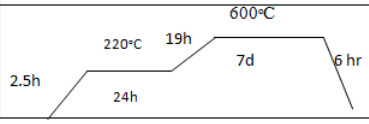	

Figure 2.2: Temperature profile for TaCoSn

2.2.2 NbFeSb

Pristine NbFeSb

Three samples of undoped NbFeSb were prepared. The method used for synthesizing these samples is described below:

• NbFeSb_01_03: The starting materials were in the form of high purity metal pieces (> 99.9% purity) purchased from Alfa Aesar and Nanoshell. These metals pieces were weighed according to the stoichiometry NbFeSb, but with 10% extra Sb added to account for the evaporation of Sb during melting. The metal pieces were loaded in an arc- melting furnace, which was evacuated and flushed with Ar gas several times before melting in an Ar atmosphere. The arc melted ingot was grounded into a fine powder. This powder was pelletized, and pellets were sealed in an evacuated quartz tube, and sintered at 850^{o}C for 7 days. The sintered pellets thus obtained had a relative mass density of about 75% (measured with respect to the theoretical density). The density of the pelletized sample was calculated using the formula ρ = m/V, where m is the mass of the pellet, which was measured using a micro balance, and V is the volume calculated by measuring the diameter and length of the pellet using a vernier calliper

• NbFeSb_02_02: For preapring this sample we used the same protocol as for the sample NbFeSb_01_03. The density of the sintered pellet was about 72%, which is close to 74% for the first sample.

• NbFeSb_03: The starting materials in this case were in the form of high purity powders (> 99.9% pure) purchased from Nanoshell and Alfa Aesar. These powders were mixed thoroughly in an argon filled glove-box, and were subsequently ball- milled for homogeneous mixing then pelletized and sealed in a quartz tube and sintered at 850^{o}C for 7 days. (pelletization was done with minimum exposure to air). In this case the sample formed was found to be brittle.

Sample Name	Methods	density
NbFeSb_0103	AM $\rightarrow$ AM$\rightarrow$ sintered at 850^{o}C (7 days)	$\sim$ 74%
NbFeSb_0202	AM$\rightarrow$ sintered at 850^{o}C (7 days)	$\sim$ 72%
NbFeSb_03	BM$\rightarrow$ sintered at 850^{o}C (7 days)	sample expanded and was brittle so density could not be calculated

Table 2.1: Pristine NbFeSb Sample preparation Summary
(AM- Arc Melting, BM- Ball Milling)

Doped and off-stoichiometric NbFeSb

A total of five Ru doped NbFeSb samples were synthesized out of which two were of Ru and Hf co-doped samples(Ru doping in $Nb_{0.86}Hf_{0.14}FeSb$); 4 samples of NbFeSb were synthesized with Nb off-stoichiometry, and finally a sample with stoichiometry $Nb_{0.86}Hf_{0.14}FeSb$ was synthesized as a control sample to access the thermoelectric performance of Ru doped samples. For the arc-melted sample 10% or 15% extra Sb was taken to compensate Sb loss during arc-melting.

• $Nb_{0.86}Hf_{0.14}Fe_{0.95}Ru_{0.05}Sb$: The precursors (with 10% extra Sb and no Ru) were arc melted, then ground (with Ru powder) and pelletized, then sealed in a quartz tube and sintered at 850 ^{o}C for 9 days and finally ice-quenched.The sample density was estimated to be about 72%

• $Nb_{0.86}Hf_{0.14}Fe_{0.97}Ru_{0.03}Sb$: The precursors (with 15% extra Sb and no Ru) were arc melted, then ground (with Ru powder) and pelletized, then sealed in a quartz tube and sintered at 850 ^{o}C for 9 days and ice-quenched. The sample density was estimated to be about 80%

• $NbFe_{0.97}Ru_{0.03}Sb$: The precursors (with 15% extra Sb and no Ru) were arc melted, then ground (with Ru powder) and pelletized, then sealed in a quartz tube and sintered at 850 ^{o}C for 9 days and ice-quenched. The density of the resulting pellet was estimated to be about 71%

• $NbFe_{0.95}Ru_{0.05}Sb$: The precursors (with 10% extra Sb) in powder form were mixed and pelletized. These pellets were arc melted then ground and pelletized then sealed in a quartz tube and sintered at 850^{o}C for 9 days and ice-quenched. The density of the sintered pellet

obtained was estimated to be about 76%

• $NbFe_{0.99}Ru_{0.01}Sb$: The precursors were ball-milled and pelletized then sealed in a quartz tube and sintered at 850^{o}C for 9 days and ice-quenched. The density of the sintered pellet could not be measured as the pellet were very brittle.

• $Nb_{1.3}FeSb$: The precursors (with 15% extra Sb) were arc melted, then ground and pelletized, then sealed in a quartz tube and sintered at 850^{o}C for 9 days and ice-quenched.The density of the sintered pellet obtained was estimated to be about 79%

• $Nb_{0.769}FeSb$: The precursors (with 15% extra Sb) were arc melted, then ground and pelletized, then sealed in a quartz tube and sintered at 850^{o}C for 9 days and ice-quenched.The density of the sintered pellet obtained was estimated to be about 64%

• $Nb_{0.95}FeSb$: The precursors (with 15% extra Sb) were arc melted, then ground and pelletized, then sealed in a quartz tube and sintered at 850^{o}C for 9 days.The density of the sintered pellet obtained was estimated to be about 75%

• $Nb_{1.1}FeSb$: The precursors (with 15% extra Sb) were arc melted, then ground and pelletized, then sealed in a quartz tube and sintered at 850^{o}C for 9 days.The density of this sample was not measured.

• $Nb_{1.05}FeSb$: The precursors (with 15% extra Sb) were arc melted, then ground and pelletized, then sealed in a quartz tube and sintered at 850^{o}C for 9 days. For this sample the density was not measured.

• $Nb_{0.86}Hf_{0.14}FeSb$: The precursors (with 15% extra Sb and no Ru) were arc melted, then ground (with Ru powder) and pelletized, then sealed in a quartz tube and sintered at 850 ^{o}C for 9 days. For this sample the density of the peletized sample was found to be around 71%

The synthesis details are summarized below in tabular form.

Sample Name	Methods	density
$Nb_{0.86}Hf_{0.14}Fe_{0.95}Ru_{0.05}Sb$	AM→ sintered at 850^{o}C (9 days)→ ice-water quenched	$\sim$ 71%
$Nb_{0.86}Hf_{0.14}Fe_{0.97}Ru_{0.03}Sb$	AM→ sintered at 850^{o}C (9 days)→ ice-water quenched	$\sim$ 80%
$NbFe_{0.97}Ru_{0.03}Sb$	AM→ sintered at 850^o C (9 days)→ ice-water quenched	$\sim$ 71%
$NbFe_{0.95}Ru_{0.05}Sb$	AM→ sintered at 850^o C (9 days)→ ice-water quenched	$\sim$ 76%
$NbFe_{0.99}Ru_{0.01}Sb$	BM→ sintered at 850^{o}C (9 days)→ ice-water quenched	sample expanded
$Nb_{1.3}FeSb$	AM→ sintered at 850^{o}C (9 days)→ ice-water quenched	$\sim$ 79%
$Nb_{0.769}FeSb$	AM→ sintered at 850^{o}C (9 days)→ ice-water quenched	$\sim$ 64%
$Nb_{0.95}FeSb$	AM→ sintered at 850^{o}C (9 days)→ ice-water quenched	$\sim$ 75%
$Nb_{1.1}FeSb$	AM→ sintered at 850^{o}C (9 days)	not measured
$Nb_{1.05}FeSb$	AM→ sintered at 850^{o}C (9 days)	not measured
$Nb_{0.86}Hf_{0.14}FeSb$	AM→ sintered at 850^{o}C (9 days)	$\sim$ 71%

Table 2.2: Sample preparation Summary
(AM- Arc Melting, BM- Ball Milling)

2.3 X-ray Diffraction

Powder X-ray Diffraction (PXRD) is a characterization technique used to check phase purity, estimate unit cell dimension and identify parasitic phases if present in the sample. PXRD works on the principle of Bragg's law ($n\lambda = 2d\sin\theta$), which gives a relation between the incident ray angle (θ) and the distance between the lattice planes (d). The instrument

consists of three parts : the X-ray tube, sample holder, and the detector. X-ray from the source tube are directed towards the sample. The sample having periodic arrangement of atoms acts as a diffraction grating and scatters the X-ray (Fig 2.3 a). Constructive interference of these diffracted rays occurs for some particular θ values (depending on the atomic planes) at which the Bragg's law is satisfied giving a peak intensity. The detector records these X-ray signals and converts them into counts, and are then shown on the computer screen.

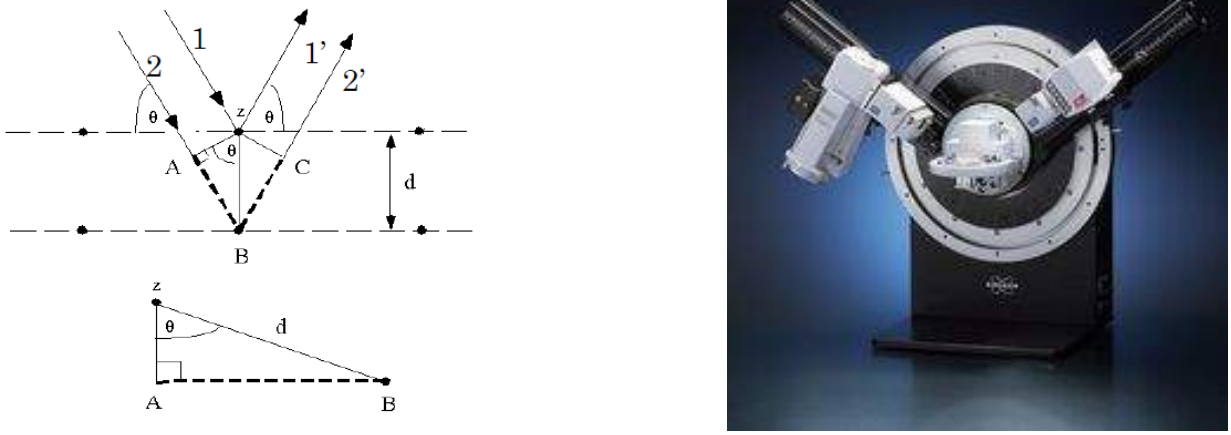

(a) Bragg's law

(b) X-ray Diffractometer

Figure 2.3: X-ray Diffraction fig (a) show the braggs law where θ is the incident angle, d is the distance between the plane, fig(b) is the image of the instrument

Source:(a)http://www.chem.latech.edu,(b)https://www.bruker.com

Powder X-ray Diffraction was done using a Bruker D8 advance diffractometer which uses Cu Kα_1 radiation of wavelength 1.5406 Å. The Kβ reflections are eliminated using a Ni-filter in the detector, while the signals due to Kα_2 are subtracted during the data processing stage after the experiment, only the signals due to Kα_1 are used for analysis. The peaks from the XRD measurement are matched using the JCPDS data available in the software (EVA) and the main phase is confirmed along with the impurity phases.

2.4 FESEM

Field Emission Scanning Electron Microscope (FESEM) analysis was done using ZEISS Gemini SEM instrument. FESEM has various application in material science like checking purity, sample morphology and elemental composition, in the case of semiconductor devices it can be used to do device cross section analysis, check construction details and also to measure coating thickness. Its working is similar to that of optical microscope. As in optical microscope the light beam is tuned using glass lenses in case of FESEM the electron beams are tuned using magnetic lenses(Fig 2.4a). The electrons coming from the electron gun (by the principle of Field Emmission Cathode) fall on the specimen . These electrons might get absorbed, reflected or generate a new electrons. These signals are detected by various detectors to give information about the surface as well as the composition of the sample.

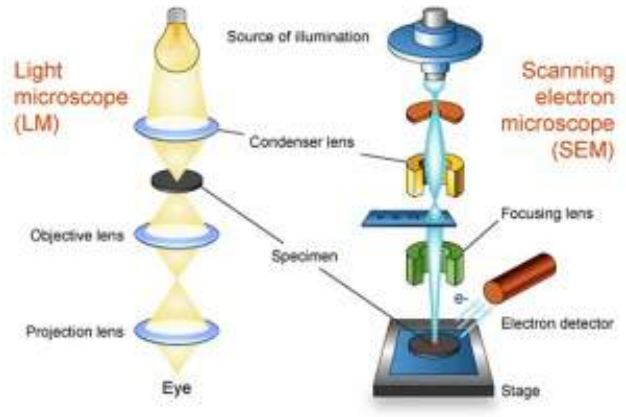

(a) compararision of FESEM and Light microscope

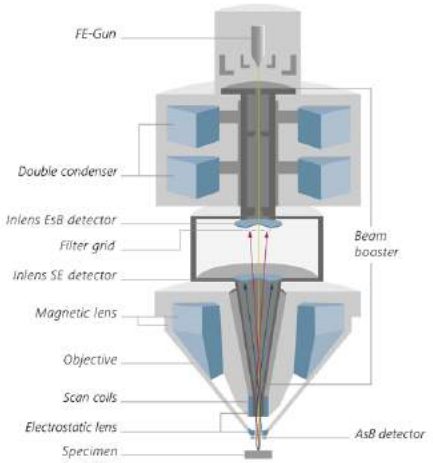

(b) FESEM

Figure 2.4: Field Emission scanning electron microscope (a) show comparision of FESEM and Light microscope, fig(b) is the image of the instrument

Source: (a) https://embryology.med.unsw.edu.au (b) https://www.zeiss.com

EDS (Energy Dispersive X-Ray Spectroscopy):

When electron beam is passed on the sample, the sample generates X-ray fluorescence which is unique to each atom. This X-ray is detected and plotted on the computer screen as a spectrum. The EDS spectrum is in the form of X-ray count with energy (in keV). Each

energy peak corresponds to an atom present in the sample. EDS is not very sensitive to lighter elements such as C or O.

2.5 Seebeck and Electrical Resistivity measuring unit

The thermoelectric measurements involve measurement of thermopower, electrical conductivity, and thermal conductivity. The first two properties (i.e, thermal power and electrical conductivity) can be measured simultaneously using LINSEIS LSR3 instrument. The Seebeck coefficient of a material is the magnitude of thermoelectric voltage generated due to temperature gradient across the material.

$$S = \frac{V_{th}}{\Delta T} \tag{2.1}$$

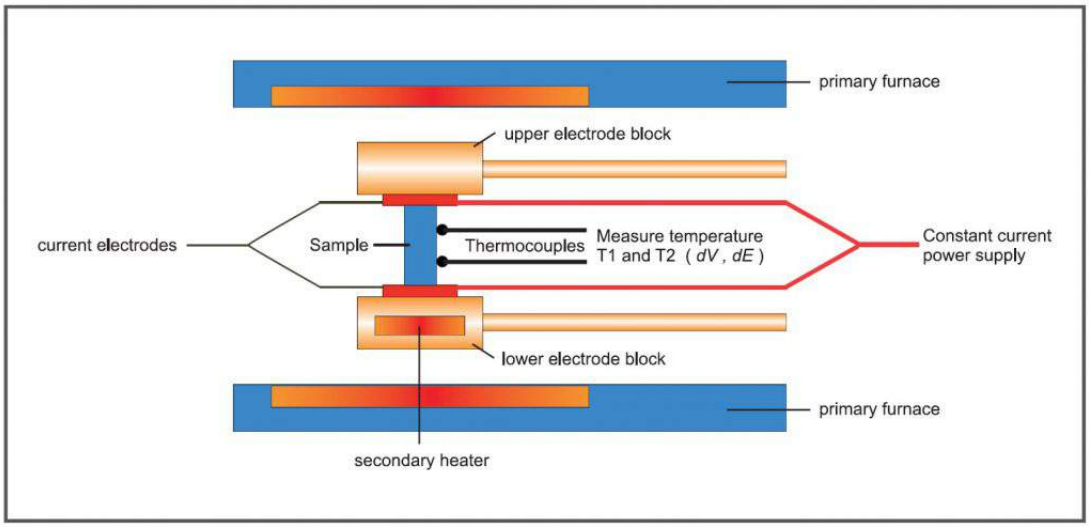

Figure 2.5: Schematics of measurement setup for measuring thermopower and electrical resistivity

PRINCIPLE: A cuboidal or cylindrical sample is placed between the two electrodes as shown in the figure 2.5. The lower electrodes contain a heating coil which is a secondary

heater. This entire setup is inside a furnace (primary furnace) which heats the sample upto a particular temperature. When this temperature is reached, the secondary heater starts and one end of the sample is heated creating a temperature gradient across the sample. Now the thermocouple begins Seebeck as well as resistance measurements.
For measurement of Seebeck coefficient the thermocouples measure the temperature T_1 and T_2 from which the temperature difference $\Delta T = T_1\text{-}T_2$ is found. Followed by the measurement of thermal electromotive force dE (or thermovoltage V_{TH}).

For measurement of resistivity dc four probe method is used. A constant current 'I' is supplied at both ends of the sample and the voltage drop dV is measured across the two thermocouples. The resistance 'R' of the sample is the ratio of voltage drop (dV) to the current 'I' through the sample. Since, the sample has a regular shape with uniform cross section, resitivity (ρ) can be calculated from the measured resistance using the formula : $\rho = R*A/l$, where A is the area of cross-section of the sample, and l is the distance between the voltage probes (the thermocouples). The electrical conductivity (σ) is then simply obtained by taking inverse of ρ.

The measurements were performed in He atmosphere till 600^oC for NbFeSb family of samples and upto 450^oC for TaCoSn samples.

2.6 Laser Flash Analyzer (LFA)

Laser Flash Apparatus measures the thermal diffusivity from which the thermal conductivity can be redily estimated provided the mass density and specific heat of the sample are known. A small disc shaped sample is placed inside a furnace that heats the sample and the surrounding. When a particular temperature is reached, the sample is subjected to a high-intensity laser pulse from the AL50 instrument for a short duration. This pulse heats the side of the sample that is towards the laser, the heat diffuses through the sample and heats the opposite surface. The rise in temperature of the rear face with time is recorded by an IR detector (detector should be continuously cooled by using liquid Nitrogen). Higher the thermal diffusivity of a sample faster the temperature rises. Various mathematical models can be employed to fit the temperature of the opposite face as a function of time in order to obtain the sample's thermal diffusivity by taking into account various corrections involved due to heat losses. The thermal diffusivity of the specimen is calculated from the following

equation. (only for adiabatic conditions)

$$\alpha = \frac{0.1388l^2}{t_{0.5}} \tag{2.2}$$

Here, α is the thermal diffusivity, l is the thickness in cm, $t_{0.5}$ is the time at 50% of the temperature increase, measured at the rare end of the specimen in seconds. If the density (ρ) of the sample is known the thermal conductivity λ can be calculated from α, ρ and Cp.

$$\lambda(T) = \alpha(T) * Cp(T) * \rho(T) \tag{2.3}$$

The measurements were done on 6 mm and 8 mm pellets till 600^oC.

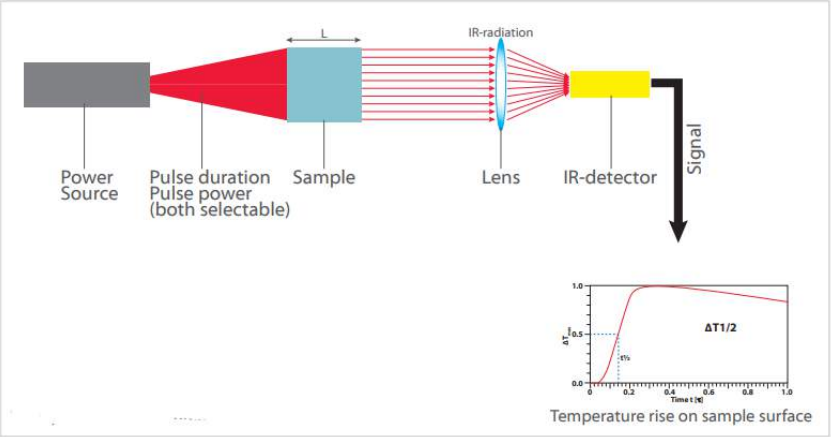

(a) LFA measurement Principle

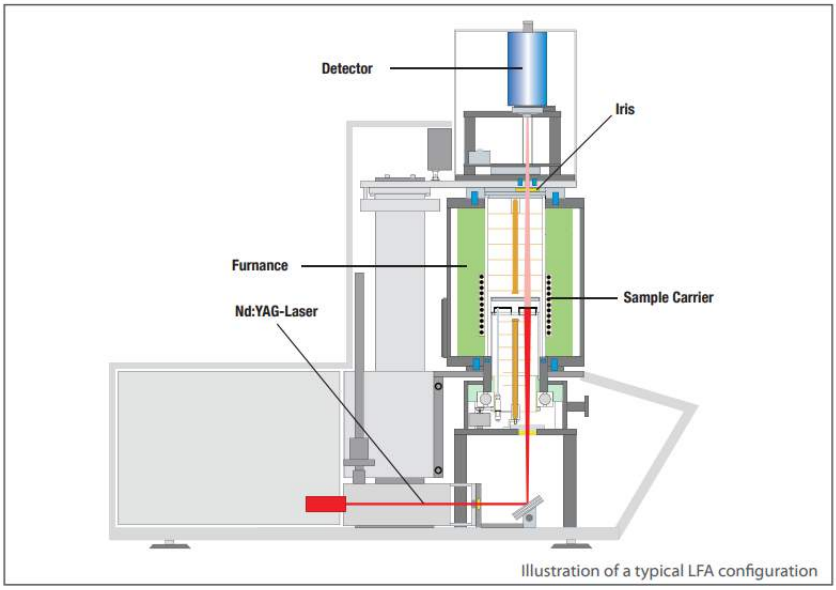

(b) Schematics of LFA setup

Figure 2.6: LFA instrument

Chapter 3

Results and Discussions

In this chapter we shall present the results of various experiments carried out during this thesis. The chapter has been organised as follows : We will first present the results on the synthesis of TaCoSn and discuss the difficulties involved in obtaining a single phase sample crystallizing with HH structure (section 3.1.1). In the next (section 3.1.2), we will then turn our attention on the HH compound NbFeSb. We shall present and discuss the PXRD and FESEM results, and provide structural details along with compositions and morphology of the samples. In the next two sections (3.3 and 3.4), the TE properties of the various synthesized samples will be shown and discussed. Finally, the main conclusion drawn from the present work appear in section 3.5.

3.1 XRD

3.1.1 TaCoSn

o TaCoSn_01: The wait at 220^{o}C and slow increase till 600^{o}C allowed Sn to melt and mix with the other precursors. Upon subsequent heating to 600^{o}C, the main phase formed with a small amount of Ta and CoSn impurities. Therefore, a second sintering was done at 1000^{o}C, however, this resulted in decomposition of the main phase. As shown in fig 3.1(a).

o TaCoSn_02: To allow Ta and CoSn to react completely, the sintering time was increased to 10 days. During this reaction, the wait duration at 220^oC was increased to 22 hrs. However, the resulting product show an increased amount of secondary phases. As shown in fig 3.1(b)

o TaCoSn_03: During the synthesis of this sample, the step at 220^oC was completely removed, and the reaction mixture was heated directly to 600^oC. The idea was to not to allow Co and Sn to react and form CoSn. However, the impurity phases persisted/increased along with the main phase. As shown in figure 3.1(c)

o TaCoSn_04: This samples was prepared in an evacuated ampoule filled inside an argon filled glove-box with almost no exposure to air, and was subsequently sintered at 600^oC. However, this sample also showed the presence of CoSn and Ta phases. As shown in fig 3.1(d).

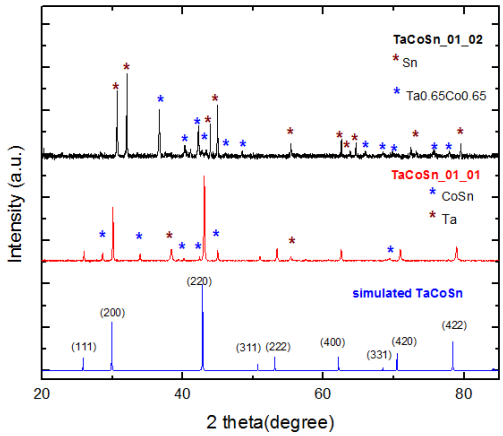

(a) XRD pattern of TaCoSn 01; blue: simulated, red: Sintering 1 (600^{o}C), black: Sintering 2 (1000^{o}C).

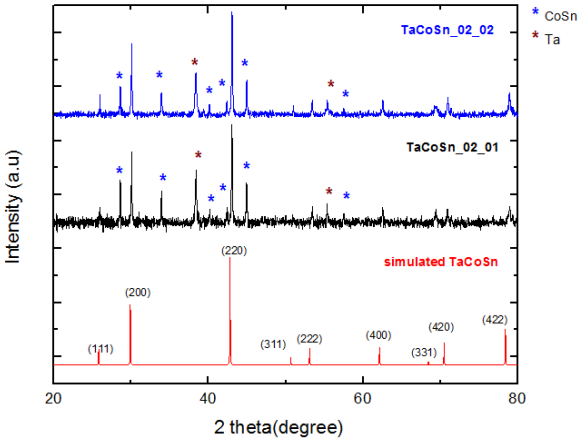

(b) XRD pattern of TaCoSn 02; red: simulated, black: Sintering 1 (600^{o}C), blue: Sintering 2 (600^{o}C)

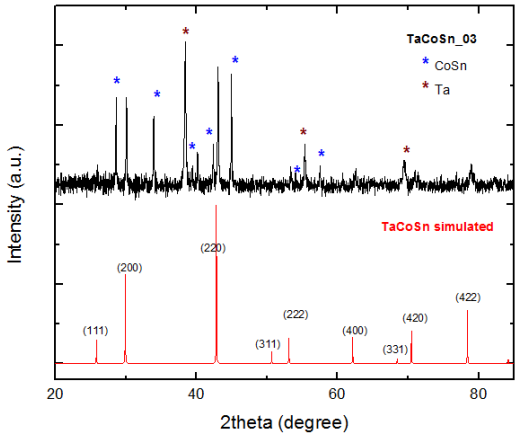

(c) XRD pattern of TaCoSn 03; red: simulated, black: Sintering 1 (600^{o}C)

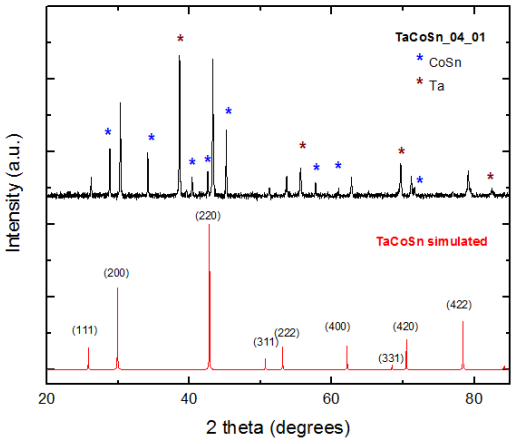

(d) TaCoSn 04; red: simulated, black: Sintering 1 (600^{o}C)

Figure 3.1: XRD pattern of TaCoSn samples

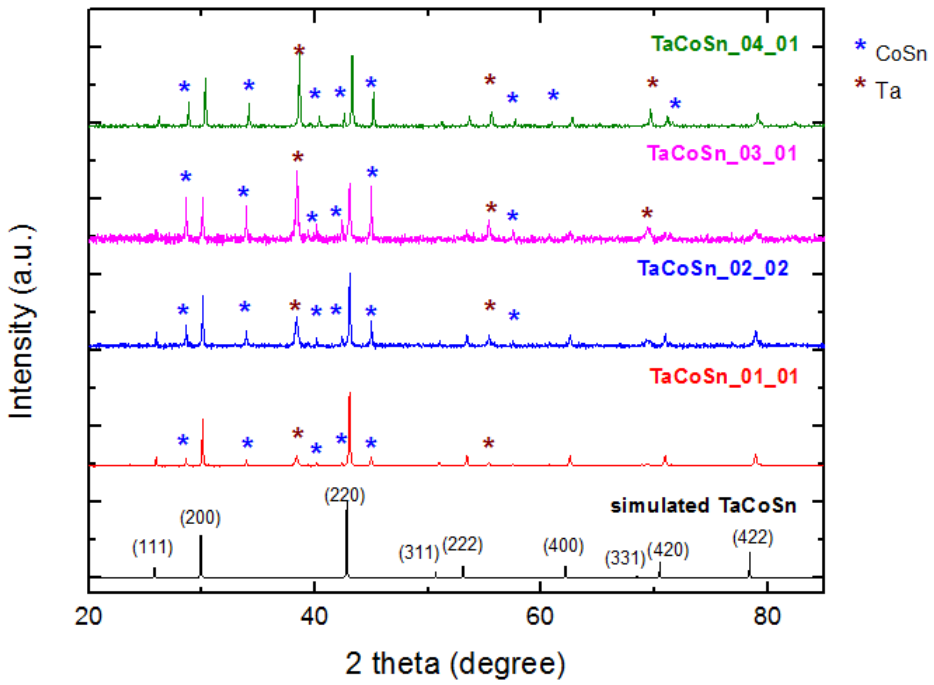

Figure 3.2: XRD comparison of all TaCoSn samples; black: simulated, red: Sintering-1 TaCoSn_01, blue: Sintering-2 TaCoSn_02, pink: Sintering-1 TaCoSn_03, green: Sintering-1 TaCoSn_04

3.1.2 NbFeSb

Three samples of NbFeSb were prepared, however one of the samples (NbFeSb_03) was too porous, and was therefore not considered for further investigation: (1) NbFeSb_01_03 showing small impurity of Nb_5Sb_4 (fig 3.3a), and (2) NbFeSb_02_02 having small impurity of FeSb and NbO_2 (fig 3.3b). Ru doped NbFeSb show FeSb and $NbSb_2$ impurities (fig 3.5), while Ru doped $Nb_{0.86}Hf_{0.14}FeSb$ samples were almost pure with samll impurity of FeSb (fig 3.6).

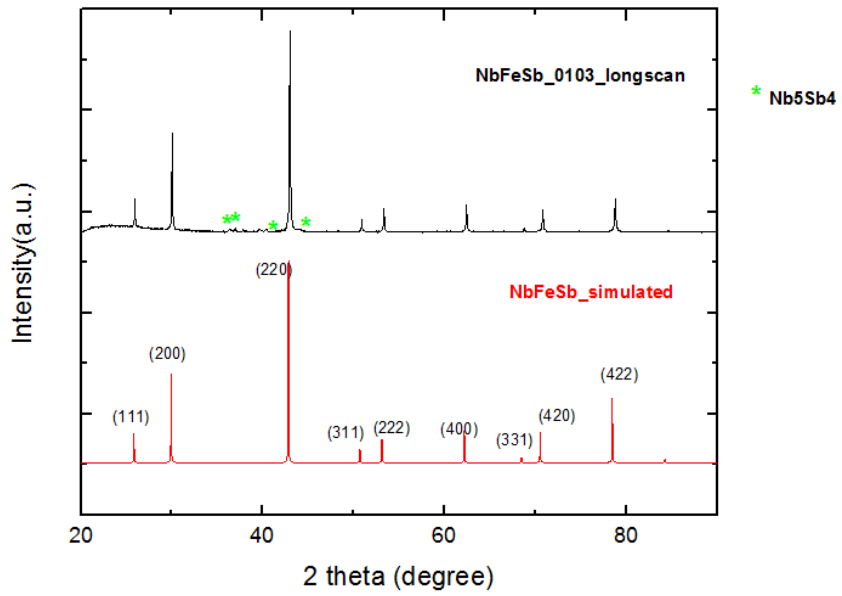

(a)

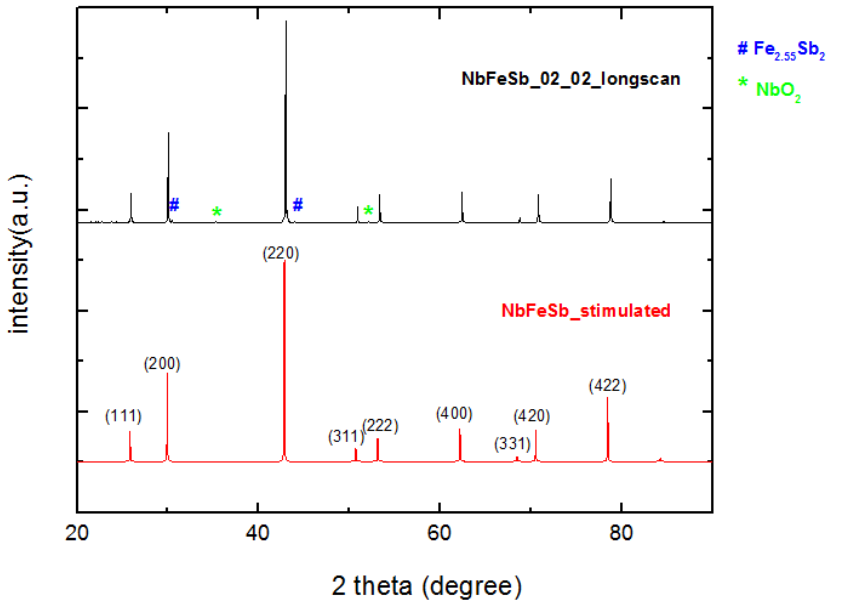

(b)

Figure 3.3: XRD pattern for pristine NbFeSb samples; (a) NbFeSb_01_03, (b) NbFeSb_02_02

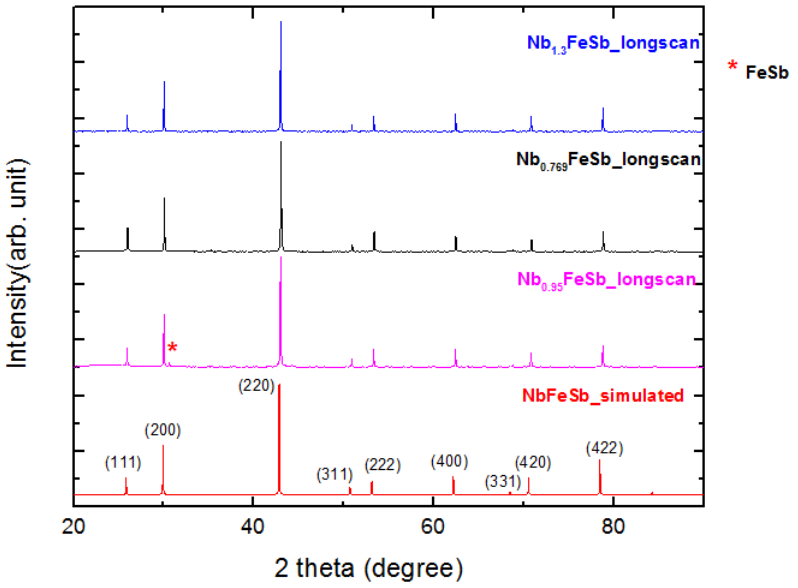

Figure 3.4: XRD pattern for Nb off-stoichiometric NbFeSb samples;

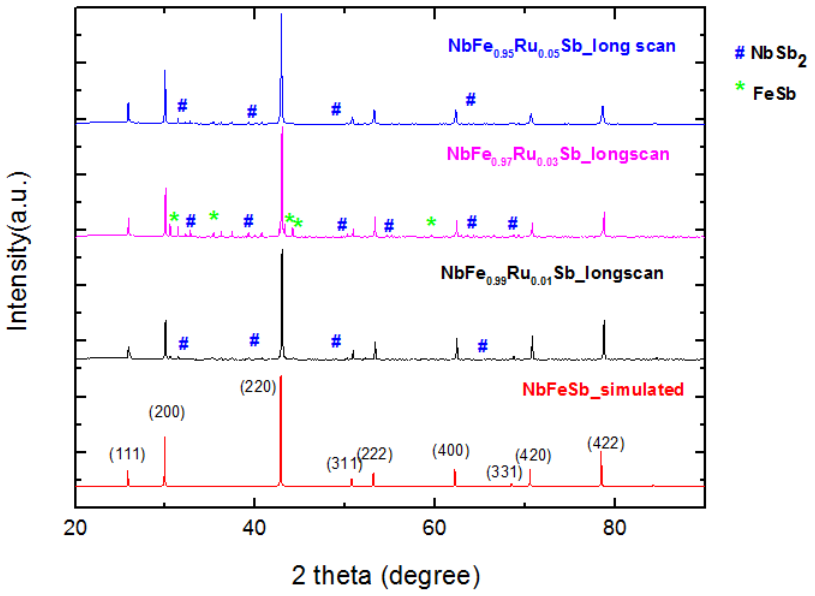

Figure 3.5: XRD pattern for Ru doping at Fe site in NbFeSb

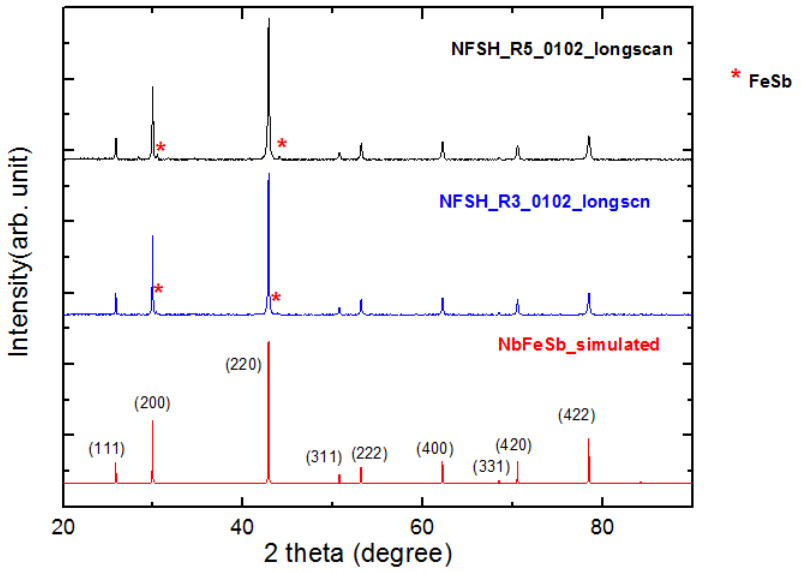

Figure 3.6: XRD pattern for Ru doping at Fe site in $Nb_{0.86}Hf_{0.14}FeSb$ (NFSH5 is $Nb_{0.86}Hf_{0.14}Fe_{0.95}Ru_{0.05}Sb$, NFSH3 is $Nb_{0.86}Hf_{0.14}Fe_{0.97}Ru_{0.03}Sb$)

Lattice parameter of all the NbFeSb samples are shown in table 3.1 . Lattice parameter increases with doping Ru. Also the samples co-doped with Ru and Hf have larger lattice parameter compared to the undoped sample, as well as the samples doped with Ru alone. However, with increasing Ru content in the co-doped samples the lattice parameter is decreases this may be due to variable size of atom based on ionic charge.

Sample Name	Lattice parameter (Å)
NbFeSb_0202	5.94654
$Nb_{0.769}FeSb$	5.94727
$Nb_{1.3}FeSb$	5.94727
$NbFe_{0.97}Ru_{0.03}Sb$	5.94807
$NbFe_{0.95}Ru_{0.05}Sb$	5.95954
$Nb_{0.86}Hf_{0.14}Fe_{0.97}Ru_{0.03}Sb$	5.96776
$Nb_{0.86}Hf_{0.14}Fe_{0.95}Ru_{0.05}Sb$	5.96399

Table 3.1: lattice parameter

3.2 FESEM

3.2.1 NbFeSb

FESEM was done on polished surface of the sample to check the composition as well as the impurity phases. Fig 3.7 show impurity of Nb_3Sb and FeNb in NbFeSb 0103 and Nb impurity in NbFeSb 0202.

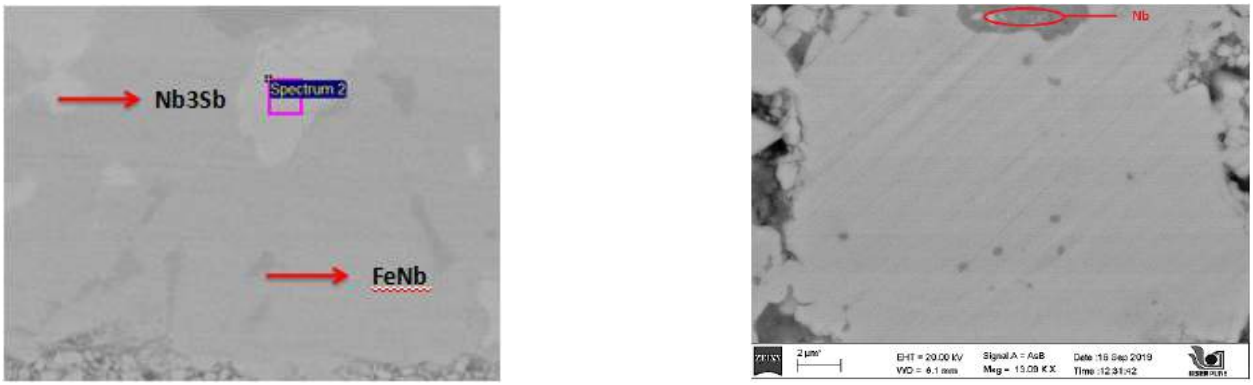

(a) NbFeSb 0103 (b) NbFeSb 0202

Figure 3.7: FESEM images of NbFeSb pristine samples

FESEM was done on off-stoichiomectric samples $Nb_{0.95}FeSb$, $Nb_{0.769}FeSb$, $Nb_{1.3}FeSb$ as seen in figure 3.8 FeSb and $NbSb_2$ impurity is seen in $Nb_{0.95}FeSb$, while only FeSb impurity is observed in $Nb_{0.769}FeSb$.

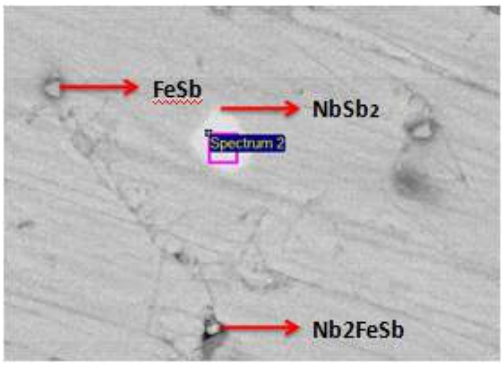

(a) $Nb_{0.95}FeSb$

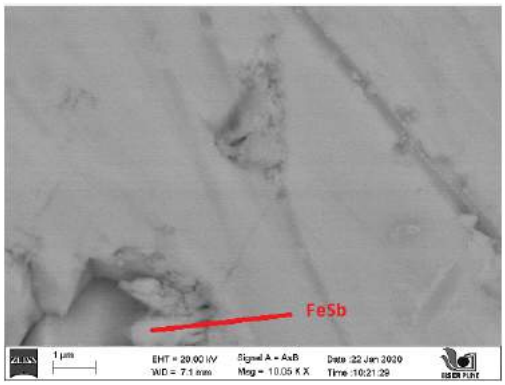

(b) $Nb_{0.769}FeSb$

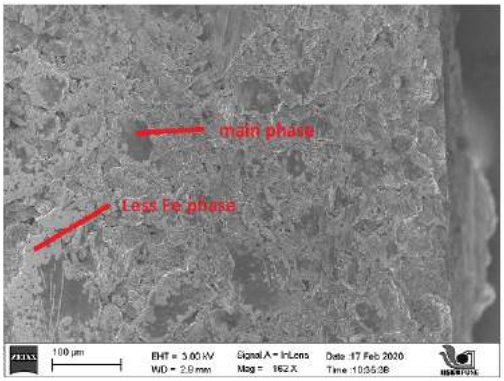

(c) $Nb_{1.3}FeSb$

Figure 3.8: FESEM image of off stoichiometric samples
(a) $Nb_{0.95}FeSb$(b) $Nb_{0.769}FeSb$ (c) $Nb_{1.3}FeSb$

FESEM done on Ru doped NbFeSb samples $NbFe_{0.95}Ru_{0.05}Sb$ and $NbFe_{0.97}Ru_{0.03}Sb$ are shown in figure 3.9, Nb and $NbSb_2$ impurity is seen in $NbFe_{0.95}Ru_{0.05}Sb$, while only $NbSb_2$ impurity is observed in $NbFe_{0.95}Ru_{0.05}Sb$.

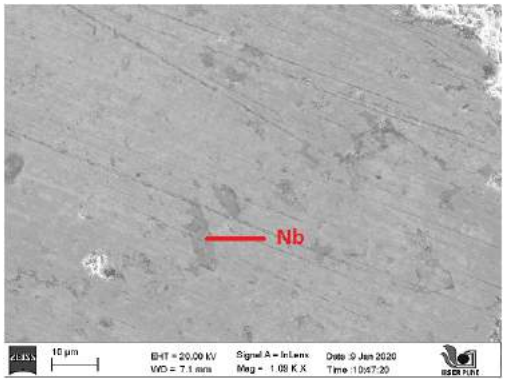

(a) $NbFe_{0.95}Ru_{0.05}Sb$

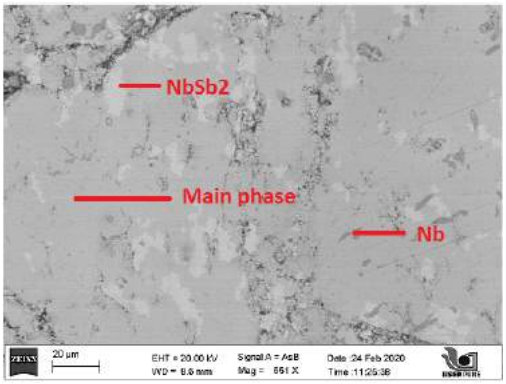

(b) $NbFe_{0.95}Ru_{0.05}Sb$

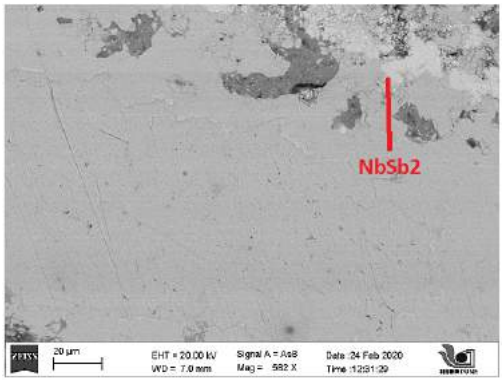

(c) $NbFe_{0.97}Ru_{0.03}Sb$

Figure 3.9: FESEM image of Ru doping at Fe site in NbFeSb samples (a),(b) $NbFe_{0.95}Ru_{0.05}Sb$ (c) $NbFe_{0.97}Ru_{0.03}Sb$

FESEM images of Ru doped $Nb_{0.86}Hf_{0.14}FeSb$ samples are shown in figure 3.10 $Nb_{0.86}Hf_{0.14}Fe_{0.97}Ru_{0.03}Sb$ and $Nb_{0.86}Hf_{0.14}Fe_{0.97}Ru_{0.03}Sb$ as seen in the figure Nb and $NbSb_2$ impurity is seen in figure FeSb impurity is observed in both the samples $NbFe_{0.95}Ru_{0.05}Sb$, while only $NbSb_2$ impurity is observed in $NbFe_{0.95}Ru_{0.05}Sb$.

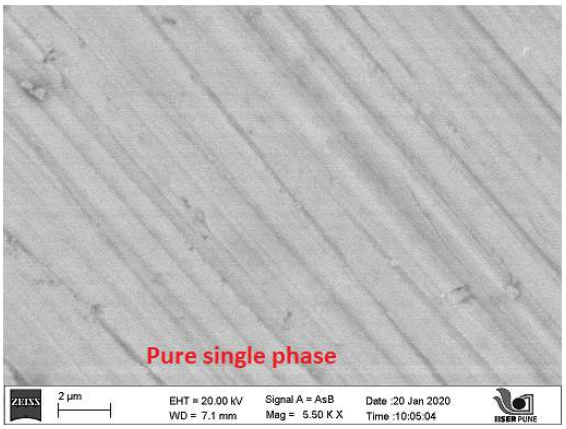

(a) $Nb_{0.86}Hf_{0.14}Fe_{0.97}Ru_{0.03}Sb$

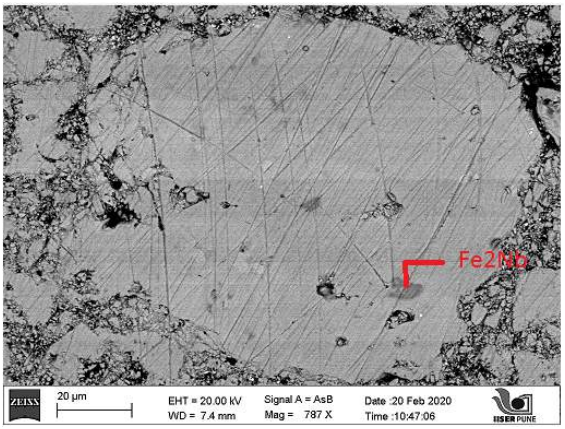

(b) $Nb_{0.86}Hf_{0.14}Fe_{0.97}Ru_{0.03}Sb$

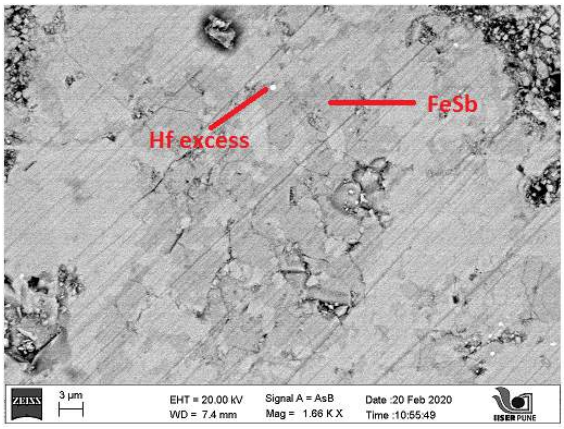

(c) $Nb_{0.86}Hf_{0.14}Fe_{0.97}Ru_{0.03}Sb$

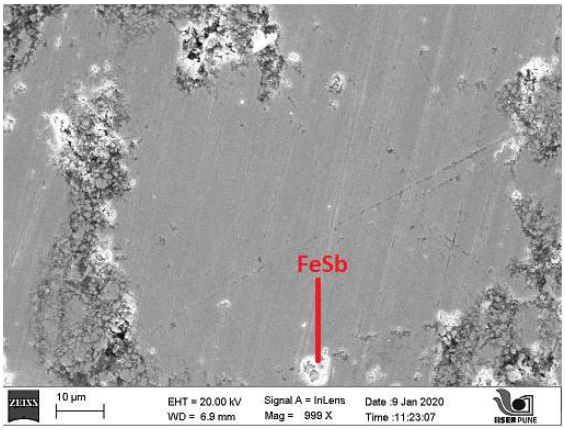

(d) $Nb_{0.86}Hf_{0.14}Fe_{0.95}Ru_{0.05}Sb$

Figure 3.10: FESEM images of Ru doping at Fe site in $Nb_{0.86}Hf_{0.14}FeSb$
(a),(b),(c) $Nb_{0.86}Hf_{0.14}Fe_{0.97}Ru_{0.03}Sb$, (d)$Nb_{0.86}Hf_{0.14}Fe_{0.95}Ru_{0.05}Sb$

In summary, TaCoSn was synthesised with minor impurity of Ta and CoSn. The impurity persisted even after further trial as can be seen in figure 3.1 and 3.2.

NbFeSb was synthesised, and doping of Ru and Hf as well as co-doping was tried. The sample with only Ru doping had significant amount of impurity. However, with Hf co-doping impurity decreased. FESEM images of samples show cracks and pores due to low density of sample. As seen in XRD as well as FESEM. Off stoichiometry of Nb in NbFeSb was also tried. Comparision of XRD and FESEM is shown in the table 3.2

Sample Name	XRD	FESEM
NbFeSb_0103	Nb_5Sb_4	Nb_3Sb , FeNb
NbFeSb_0202	FeSb, NbO_2	Nb
$Nb_{0.769}FeSb$	FeSb	FeSb
$Nb_{1.3}FeSb$	small impurity of Nb_5Sb_4, Nb_3Sb	Nb-Sb phase , Nb
$Nb_{0.95}FeSb$	FeSb	Nb
$NbFe_{0.97}Ru_{0.03}$	FeSb, $NbSb_2$	FeSb, $NbSb_2$, Nb
$NbFe_{0.95}Ru_{0.05}$	$NbSb_2$	Nb, $NbSb_2$
$Nb_{0.86}Hf_{0.14}Fe_{0.97}Ru_{0.03}Sb$	FeSb	FeSb, Hf
$Nb_{0.86}Hf_{0.14}Fe_{0.95}Ru_{0.05}Sb$	FeSb	FeSb, no Ru in matrix

Table 3.2: Summary of impurity phases in various samples as detected using Powder X-ray diffraction and FESEM techniques

Sample Name	Stoichiometry				
	Nb	Fe	Sb	Ru	Hf
NbFeSb_02_02	1.18	1	1.1		
NbFeSb_01_03	1.3	1	0.89		
N0.95FeSb	1.15	1	1.09		
Nb0.769FeSb	1.16	1	1.1		
Nb1.3FeSb	1.35	1	1.15		
NFSR3	1	1.05	1.2	0.04	
NFSR5	1	0.837	0.98	0.05	
NFSHR3	0.91	0.89	1	0.03	0.11
NFSHR5	0.96	0.87	1	0.03	0.08

Figure 3.11: FESEM Stoichiometric analysis of all NbFeSb samples; Here nfsr3 is for $NbFe_{0.97}Ru_{0.03}Sb$, nfsr5 is $NbFe_{0.95}Ru_{0.05}Sb$, nfshr3 is for $Nb_{0.86}Hf_{0.14}Fe_{0.97}Ru_{0.03}Sb$ and nfshr5 is for $Nb_{0.86}Hf_{0.14}Fe_{0.95}Ru_{0.05}Sb$

(If we see the stoichiometry of NFSHR5 it is possible that Hf did not go into the matrix. Hence the decrease in Lattice parameter in table 3.1 and decreased conductivity futher in LSR measurement fig 3.16)

3.3 TE Measurements: Thermopower, Electrical conductivity and PF

3.3.1 TaCoSn

As shown in the previous section, TaCoSn forms with a parasitic phase CoSn and some unreacted Ta. Increasing the sintering duration or carrying out second sintering at same or higher temperature only made the sample worse. However, since TaCoSn is a relatively much less studied sample, we decided to measure the TE properties of one of our TaCoSn samples. The resistivity and thermopower measurements were carried out on sample TaCoSn_03. The results are shown in Fig. 3.12. Near room temperature it shows a reasonably high electrical conductivity of about 2600 S/cm. With increasing temperature the conductiviy decreases which is a behaviour typical of degenerate semiconductor. The thermopower near room temperature is negative, about -30 microvolt per Kelvin, which is not as high as expected based on theoretical calculation by Wang *et.al*[7]. The power factor is plotted in Fig.3.12(c). It is close to 2 μW/cmK^2, which is about an order of magnitude smaller than what is normally found for good TE materials.

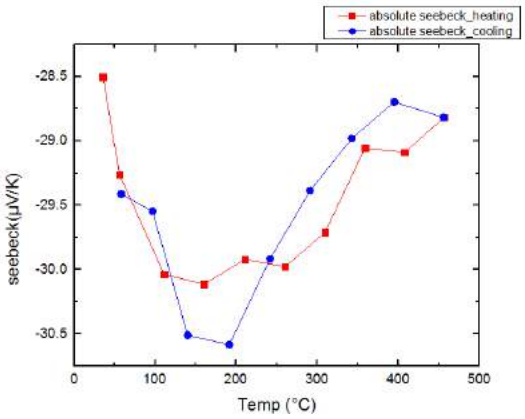

(a) Seebeck of TaCoSn 03

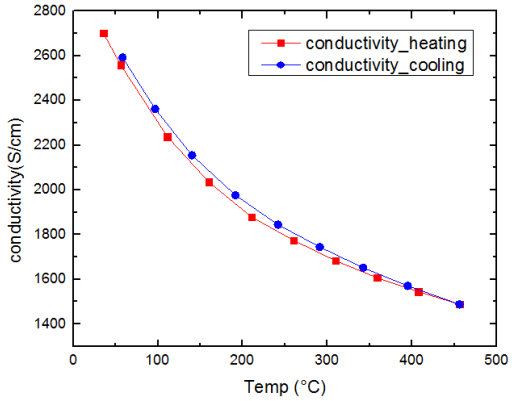

(b) conductivity TaCoSn 03

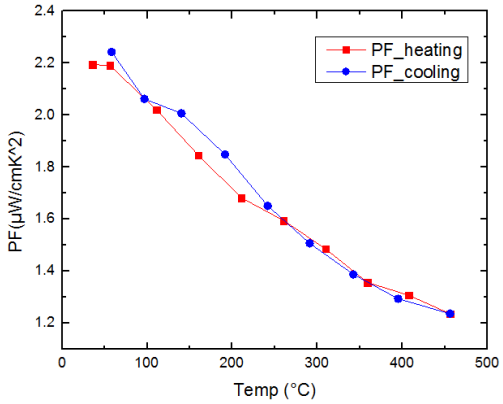

(c) PF of TaCoSn 03

Figure 3.12: LSR measurements of TaCoSn 03

3.3.2 NbFeSb

Pristine NbFeSb

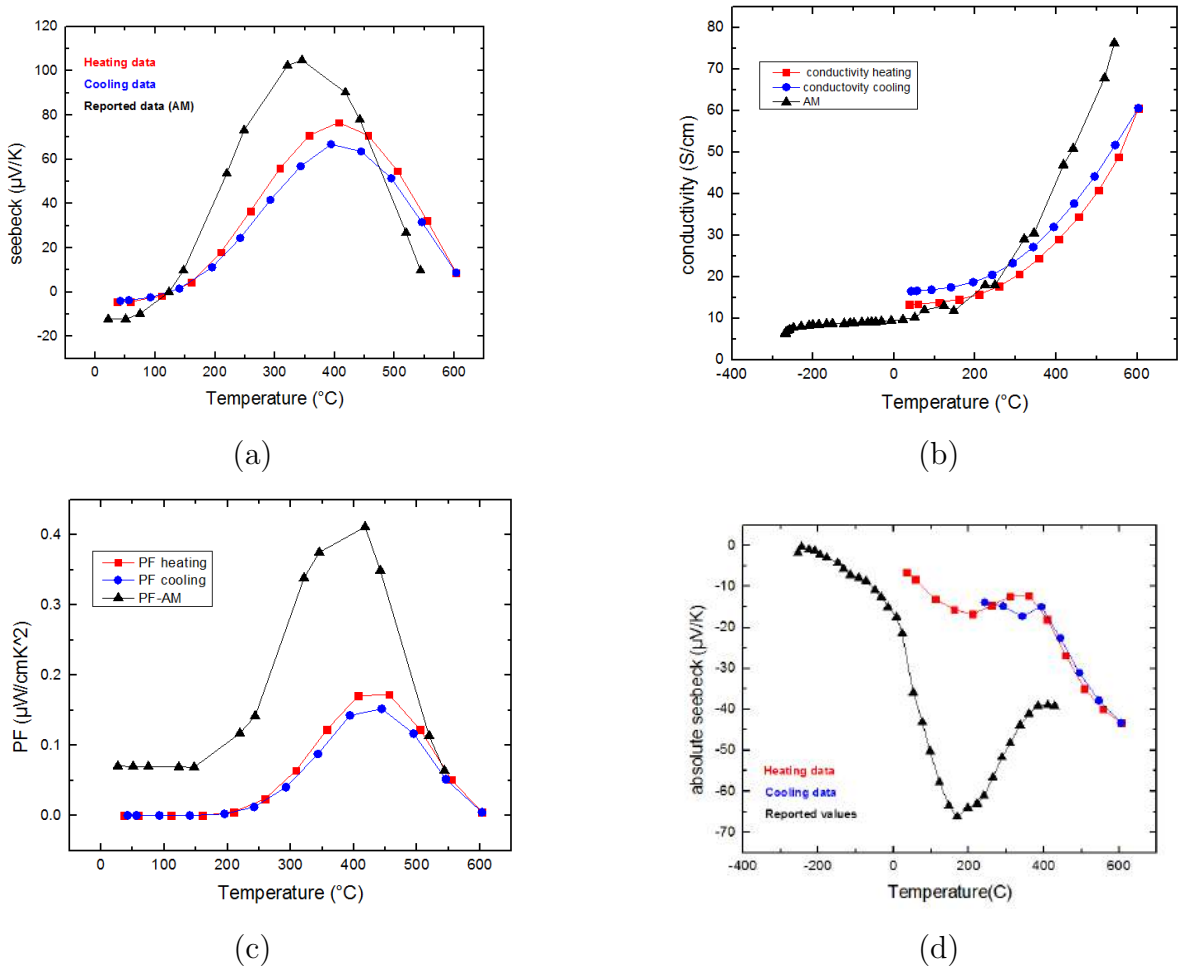

Figure 3.13: TE measurements of NbFeSb samples; (a), (b), and (c) are Thermopower, Electrical conductivity, and PF respectively for NbFeSb_02_02 sample and (d) is Thermopower of NbFeSb_01_03 sample. Here, reported values refers to ref. [20] reports of TE measurement, and AM refers to ref. [1] work

Figure 3.13 shows the TE measurements for the two pristine samples NbFeSb_02_02 and NbFeSb_01_03. For sample NbFeSb_02_02: The behavior of the Seebeck coefficient, electrical conductivity, and PF matches with the reported data by A. Tavassoli *et. al*[1]. The thermopower of our sample changes from negative to positive at $\sim$ 150 ^{o}C reaching a maxi-

mum of 76 μV/K at 400^{o}C. The maximum thermopower (76 μV/K at 400^{o}C) is smaller than the value reported by A. Tavassoli *et. al* ($\sim$100 μV/K) as shown in fig 3.13(a). The electrical conductivity agrees well with the reported work[1]. At the same time, due to slightly lower values of Seebeck coefficient, the PF is found to have degraded [fig 3.13 (a),(b),(c)]. Figure 3.13 (d) shows the measured Seebeck coefficient of another pristine sample NbFeSb_01_03. Seebeck coefficient for this sample unexpectedly showed a negative sign indicating n-type behavior. Similar n-type behavior has been recently reported by D. Hobbis *et. al*[20]. They have attributed the negative thermopower to anti-phase boundary (APB) formation in their sample. According to them APB lead to additional charge donation by Fe that is adjacent to the APB leading to local disruption of 18-VEC and hence, charge doping in the system. The XRD of NbFeSb samples after arc melting showed high amount of parasitic sites which disappear after sintering. This indicated that during arc melting there is high probability of some Fe-Sb phases with low boiling point to have evaporated, resulting in stoichiometry changes in the final sample. So, we believe that in NbFeSb_01_03 sample, the n-type behavior might be due to off stoichiometry. Hence, $Nb_{1+x}FeSb$ samples were studied. The results for $Nb_{1+x}FeSb$ samples will be discussed shortly.

Off stoichiometric NbFeSb

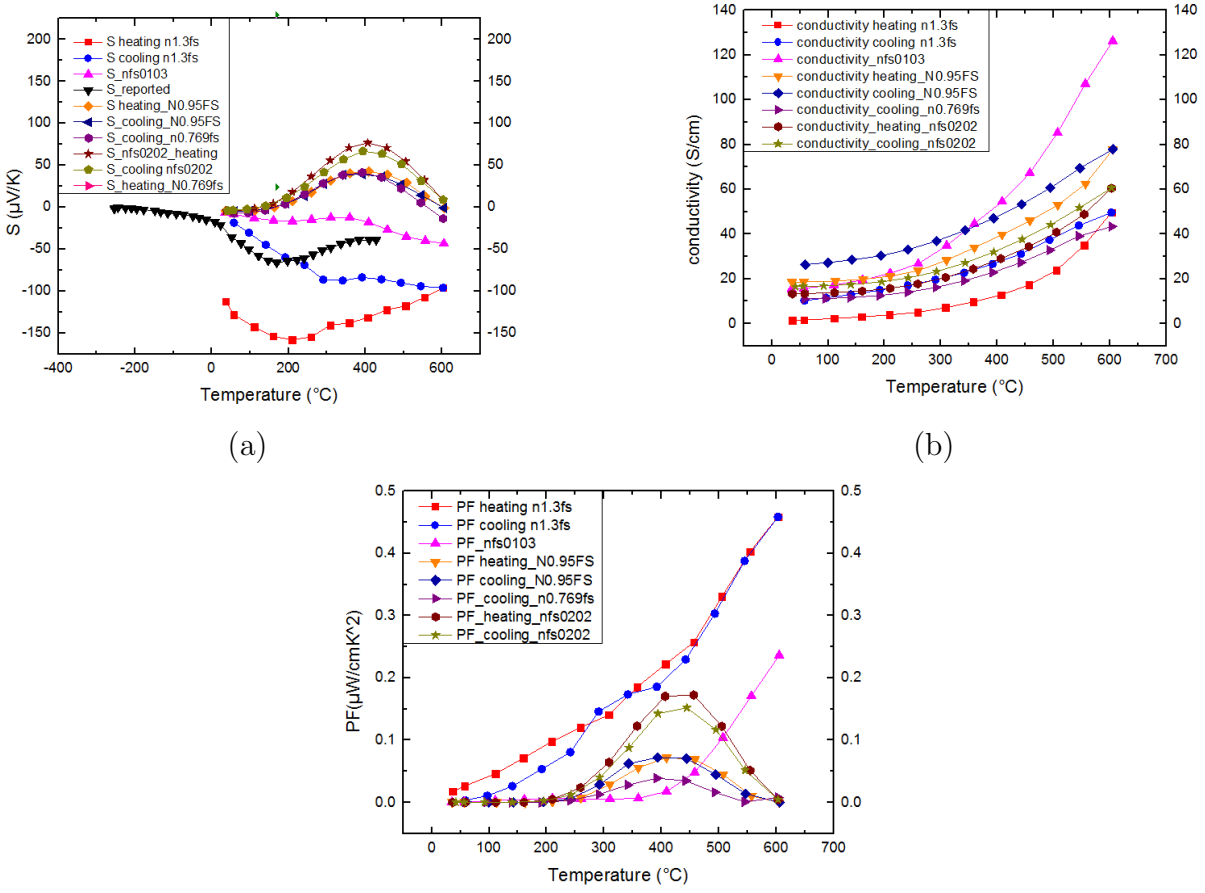

Figure 3.14: TE measurements of $Nb_{1+x}FeSb$ samples (a) Seebeck Coefficient, (b) Electrical conductivity, (c) Power Factor; Here, n1.3fs refers to the Nb excess sample $Nb_{1.3}FeSb$ [x=0.3], N0.95FS is $Nb_{0.95}FeSb$[x=-0.05], N0.769FS is $Nb_{0.769}FeSb$ [x=-0.23], while NFS0103 and NFS0202 are the pristine sample NbFeSb_01_03 and NbFeSb_02_02 [x=0] respectively and reported refers to ref. [20] reports of negative S

As mentioned earlier to investigate the unexpected negative sign for pristine NbFeSb_01_03 sample, $Nb_{1+x}FeSb$ samples were studied. Here, we discuss the results obtained from the LSR measurements performed on $Nb_{1+x}FeSb$ samples (x=-0.23,-0.05, 0.3), and compare them with NbFeSb_01_03 and NbFeSb_02_02 [x=0] (figure 3.14). Similar to NbFeSb_01_03, $Nb_{1.3}FeSb$ showed negative sign for thermopower over the entire temperature range [fig 3.13(a)] and achieved maximum thermopower of -158 μV/K at $\sim$ 200^{o}C reasonably higher

as compared to NbFeSb_01_03 and litrature reports (-67 μV/K at $\sim$ 170^{o}C)[20]. The electrical conductivity of $Nb_{1.3}$FeSb and NbFeSb_01_03 is $\sim$ 20 S/cm near room temperature, as consistant with the semiconducting behaviour the σ increases with temperature reaching a maximum of 50 S/cm and 125 S/cm respectively at 600^{o}C [fig 3.13(b)]. The improved thermopower of $Nb_{1.3}$FeSb as compared to NbFeSb_01_03 overpowers the degraded σ resulting in higher PF of $Nb_{1.3}$FeSb. Both samples show increasing behavior of PF with temperature contradictory to the behaviour shown by NbFeSb_02_02 and Nb_{1+x}FeSb samples (x= -0.23, -0.05) i.e Nb deficient samples. The maximum PF reached for $Nb_{1.3}$FeSb and NbFeSb_01_03 is 0.45μW/cmK^2 and 0.23μW/cmK^2 respectively at $\sim$600^{o}C.

All the Nb_{1+x}FeSb (x= -0.23, -0.05, 0) samples show TE behavior comparable to the results reported by A. Tavassoli[1]. The maximum thermopower for Nb deficient sample is observed to be 40 μV/K about two times lower than the reported and x=0 sample [fig 3.14(a)], thus PF seems to degrade with Nb deficiency.

$Nb_{1.3}$FeSb has almost reproduced the NbFeSb_01_03 results. From this we can infer that excess Nb in the stoichometric NbFeSb samples can lead to p to n type conversion in NbFeSb. (We had planned to further confirm if excess Nb in stoichiometry is truly responsible for the negative thermopower and to see the effect on TE properties mostly on thermopower, two more samples (x= 0.05, 0.1) were prepared, but, LSR measurements remain to be performed.)

Ru doping at Fe site in NbFeSb

To get an understanding of the effect of Ru doping in NbFeSb five Ru doped samples were synthesised: Three with Ru doping at Fe site in NbFeSb ($NbFe_{0.95}Ru_{0.05}Sb$, $NbFe_{0.97}Ru_{0.03}Sb$, $NbFe_{0.99}Ru_{0.01}Sb$) and two samples of Ru doping at Fe site in $Nb_{0.86}Hf_{0.14}$FeSb. Here, we will discuss the results for Ru doping at Fe site in NbFeSb. Characterisation analysis of these samples show significant amount of impurity phases of $NbSb_2$ and FeSb. Since, Ru doping in NbFeSb has not been studied, and also to further compare it's TE property behaviour with rather pure Hf and Ru co-doped samples, we measured these samples. Seebeck and resistivity measurements were performed on $NbFe_{0.95}Ru_{0.05}Sb$ and $NbFe_{0.97}Ru_{0.03}Sb$ ($NbFe_{0.99}Ru_{0.01}Sb$ sample expanded) and is shown in figure 3.14. The Seebeck measurement (fig 3.15(a) of $NbFe_{0.97}Ru_{0.03}Sb$ shows similar behaviour to NbFeSb 0202, while, $NbFe_{0.97}Ru_{0.03}Sb$ shows a negative sign throughout the temperature range. Electrical conductivity measurement is

lowest for $NbFe_{0.97}Ru_{0.03}Sb$ ($\sim$ 50 S/cm at 600^{o}C) followed by the pristine sample ($\sim$ 60 S/cm at 600^{o}C) and the maximum for $NbFe_{0.95}Ru_{0.05}Sb$($\sim$ 80S/cm at 600^{o}C).

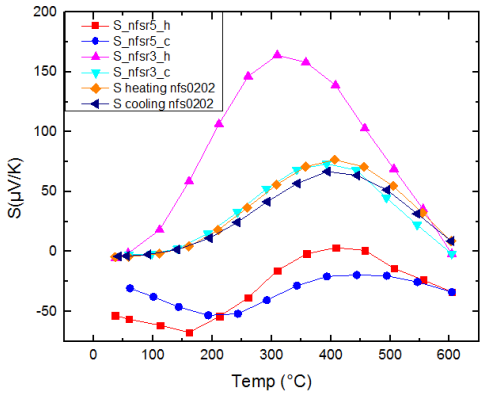

(a)

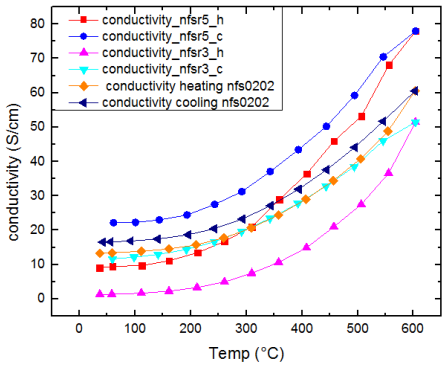

(b)

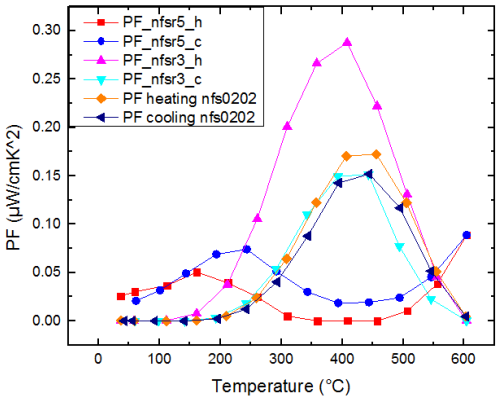

(c)

Figure 3.15: TE measurements of Ru doped samples (a) Thermopower, (b) Conductivity, and (c) PF ; Here, nfsr3 is for $NbFe_{0.97}Ru_{0.03}Sb$, nfsr5 is $NbFe_{0.95}Ru_{0.05}Sb$, nfs0202 is NbFeSb_02_02 and 'h' stands for heating data while 'c' for cooling data

Ru doped at Fe site in $Nb_{0.86}Hf_{0.14}FeSb$

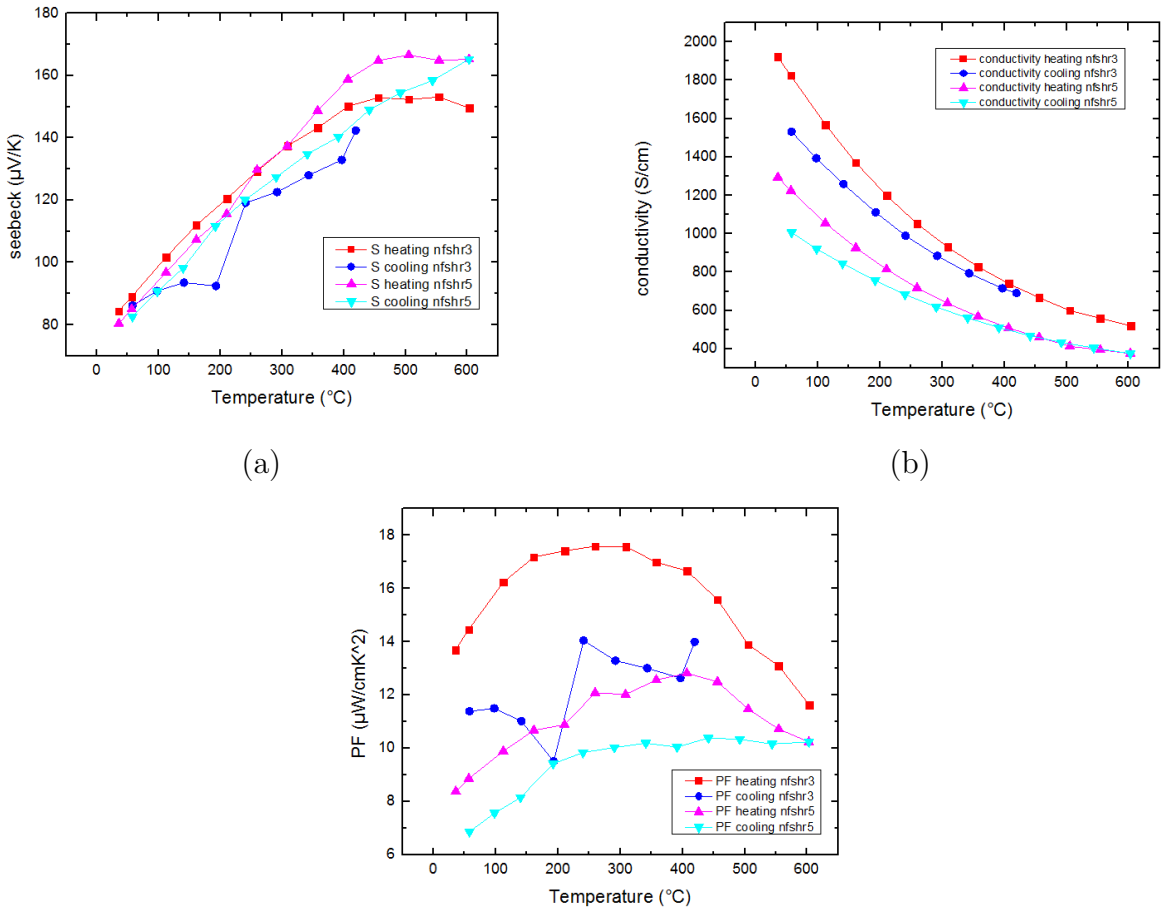

Figure 3.16: TE measurements for Ru doping at Fe site in $Nb_{0.86}Hf_{0.14}FeSb$ samples (a) Thermopower measurement, (b) Conductivity and (c) PF; Here, nfshr3 is for $Nb_{0.86}Hf_{0.14}Fe_{0.97}Ru_{0.03}Sb$, nfshr5 is for $Nb_{0.86}Hf_{0.14}Fe_{0.95}Ru_{0.05}Sb$

Here, we will discuss TE property measurements of Ru doping in $Nb_{0.86}Hf_{0.14}FeSb$ samples; two samples $Nb_{0.86}Hf_{0.14}Fe_{0.95}Ru_{0.05}Sb$ and $Nb_{0.86}Hf_{0.14}Fe_{0.97}Ru_{0.03}Sb$ were studied. XRD and FESEM analysis show that the above samples have crystallized in HH phase with negligible amount of FeSb impurity. The results of TE measurements are shown in figure 3.16. In contrast to our Ru doped NbFeSb samples and pristine NbFeSb, the thermopower for Hf and Ru co-doped samples show increasing trend with temperature which is generally reported for Hf doped NbFeSb samples[1][2]. Near room temperature the thermopower is $\sim$

80 μV/K and increases to $\sim$ 160 μV/K at 600^{o}C for both. While we observe a significant decrease in σ with Ru doping, we believe this might be due to mass fluctuation affect on mobility. The power factor is observed to decrease with Ru doping due to depleated conductivity. However, σ values for our sample are much lower than than those reported by Fu*et.al* almost 4 to 5 times. Though the thermopower is comparable to the litreature values, the decreased conductivity of the sample results in a much lower PF than that reported for Hf doped NbFeSb.

3.4 TE Measurements: Thermal conductivity and ZT for doped NbFeSb samples

3.4.1 Thermal conductivity

Thermal conductivity measurements performed on 6 mm or 8 mm pellets of Ru doped NbFeSb and $Nb_{0.86}Hf_{0.14}FeSb$ samples are shown in figure 3.17. The thermal conductivity values for $Nb_{0.86}Hf_{0.14}FeSb$ sample was also measured and are around 1 to 2 W/mK over the entire temperature range. We expected Ru doping to result in mass fluctuation and decrease the thermal conductivity. However, the thermal conductivity of all the Ru doped samples (Ru doping in NbFeSb and $Nb_{0.86}Hf_{0.14}FeSb$) increased as compared to the $Nb_{0.86}Hf_{0.14}FeSb$ measured sample. We also observe that all our prepared samples have substantially lower κ values than those reported by A. Tavassoli *et.al*[1] and Fu *et.al*[2]. This reduction in thermal conductivity might also be due to low density (table 2.2), which is a crucial factor in thermal conductivity calculations.

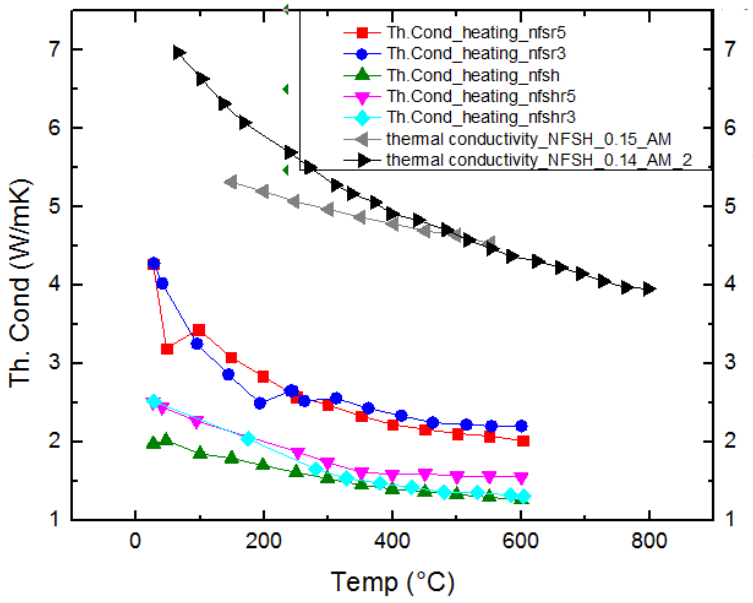

Figure 3.17: Thermal conductivity of all doped NbFeSb samples; Here nfsr3 is for $NbFe_{0.97}Ru_{0.03}Sb$, nfsr5 is $NbFe_{0.95}Ru_{0.05}Sb$, nfsh is for $Nb_{0.86}Hf_{0.14}FeSb$, nfshr3 is for $Nb_{0.86}Hf_{0.14}Fe_{0.97}Ru_{0.03}Sb$ and nfshr5 is for $Nb_{0.86}Hf_{0.14}Fe_{0.95}Ru_{0.05}Sb$, NFSH0.15_AM is reported data for $Nb_{0.85}Hf_{0.15}FeSb$ by Tavassoli *et.al.*[1], NFSH_0.14_AM_2 is reported data for $Nb_{0.86}Hf_{0.14}FeSb$ by Fu *et.al.*[2]

3.4.2 ZT

Comparing the ZT values obtained in this work with the literature data reported for samples with composition similar to $Nb_{0.86}Hf_{0.14}FeSb$ shown in figure 3.18, one finds that the ZT values for $Nb_{0.86}Hf_{0.14}Fe_{0.97}Ru_{0.03}Sb$ is comparable to those reported for $Nb_{0.86}Hf_{0.14}FeSb$ [1][2]. While, $Nb_{0.86}Hf_{0.14}Fe_{0.95}Ru_{0.05}Sb$ sample reports decrease in ZT. Eventhough, the samples report very low PF the ZT is comparable to the literature data because of tremendous decrease in κ (fig 3.17). Maximum ZT obtained for $Nb_{0.86}Hf_{0.14}Fe_{0.97}Ru_{0.03}Sb$ is ~ 0.88 and decreased to ~ 0.5 for $Nb_{0.86}Hf_{0.14}Fe_{0.97}Ru_{0.03}Sb$ at 900K.

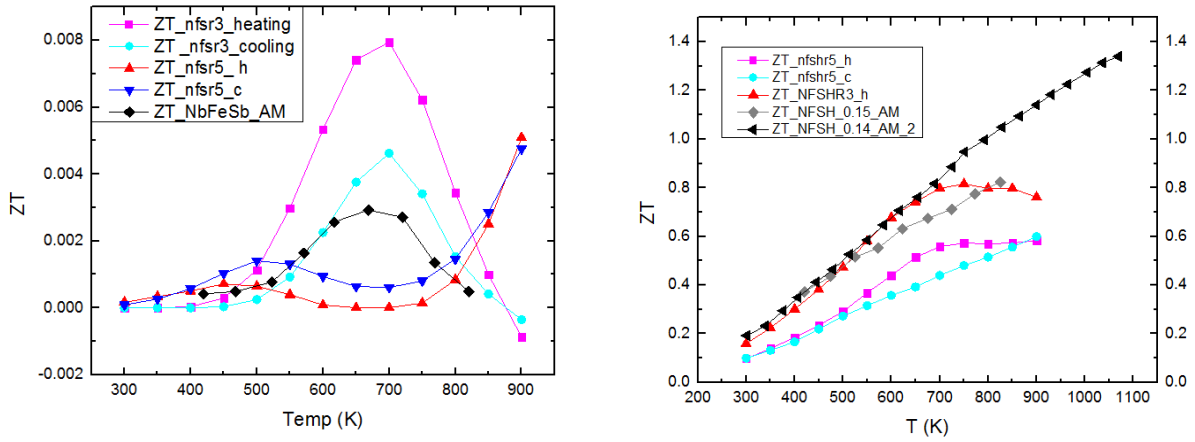

(a) (b)

Figure 3.18: ZT of doped NbFeSb samples; (a) ZT for Ru doping at Fe site in NbFeSb (b) ZT for Ru doping at Fe site in $Nb_{0.86}Hf_{0.14}FeSb$ samples. Here, nfsr3 is for $NbFe_{0.97}Ru_{0.03}Sb$, nfsr5 is $NbFe_{0.95}Ru_{0.05}Sb$,nfshr3 is for $Nb_{0.86}Hf_{0.14}Fe_{0.97}Ru_{0.03}Sb$ and nfshr5 is for $Nb_{0.86}Hf_{0.14}Fe_{0.95}Ru_{0.05}Sb$.While, 'h' stands for heating data and 'c' for cooling data.

Chapter 4

Conclusion

TaCoSn_01 formed with small impurities of Ta and CoSn after second sintering at 1000 ^{o}C the sample decomposed. Further, attempt at sample formation resulted in increased impurities. LSR measurements performed on TaCoSn_03, showed different behavior than reported due to high impurity.

The negative thermopower obtained for one of the pristine sample (NbFeSb_0103) has been reproduced by off-stoichiometric sample with improved thermopower and PF than NbFeSb_0103. Suggesting Nb excess in stoichiometric NbFeSb might be responsible for the unexpected transition to n-type in NbFeSb. Ru doping study on NbFeSb revealed that mass fluctuation effect of Ru doping in $Nb_{0.86}Hf_{0.14}FeSb$ is more prominant on electron mobility than thermal conductivity thus decreasing the ZT from $\sim$ 0.88 for 3% doping to $\sim$ 0.5 for 5% doping near 900 K.

Bibliography

[1] Tavassoli, A. et al. On the Half-Heusler compounds Nb1-xTi,Zr,HfxFeSb: Phase relations, thermoelectric properties at low and high temperature, and mechanical properties. Acta Mater. 135, 263–276 (2017).

[2] Fu, C. et al. Realizing high figure of merit in heavy-band p-type half-Heusler thermoelectric materials. Nat. Commun. 6, 4–10 (2015).

[3] Ren, W. et al. Ultrahigh Power Factor in Thermoelectric System Nb0.95M0.05FeSb (M = Hf, Zr, and Ti). Adv. Sci. 5, (2018).

[4] Yu, J., Xia, K., Zhao, X. Zhu, T. High performance p-type half-Heusler thermoelectric materials. J. Phys. D. Appl. Phys. 51, aaaa58 (2018).

[5] Mao, J. et al. Advances in thermoelectrics. Adv. Phys. 67, 69–147 (2018).

[6] Zhou, J. et al. Large thermoelectric power factor from crystal symmetry-protected nonbonding orbital in half-Heuslers. Nat. Commun. 9, 1–9 (2018).

[7] Wei, J. Wang, G. Thermoelectric and optical properties of half-Heusler compound TaCoSn: A first-principle study. J. Alloys Compd. 757, 118–123 (2018).

[8] Li, S. et al. N-Type TaCoSn-Based Half-Heuslers as Promising Thermoelectric Materials. ACS Appl. Mater. Interfaces 11, 41321–41329 (2019).

[9] Zakutayev, A. et al. Theoretical prediction and experimental realization of new stable inorganic materials using the inverse design approach. J. Am. Chem. Soc. 135, 10048–10054 (2013).

[10] Casper, F., Graf, T., Chadov, S., Balke, B. Felser, C. Half-Heusler compounds: Novel materials for energy and spintronic applications. Semicond. Sci. Technol. 27, (2012).

[11] H.J. Goldsmid, Introduction to Thermoelectricity, Vol. 121, Springer, Heidelberg, 2009.

[12] Heremans, J. P. et al. Enhancement of Thermoelectric of the Electronic Density of States. Science (80-.). 321, 1457–1461 (2008).

[13] Mahan, G. D. Sofo, J. O. The best thermoelectric. Proc. Natl. Acad. Sci. U. S. A. 93, 7436–7439 (1996).

[14] Zhang, Q. et al. Enhancement of thermoelectric figure-of-merit by resonant states of aluminium doping in lead selenide. Energy Environ. Sci. 5, 5246–5251 (2012).

[15] C.M. Jaworski, V. Kulbachinskii and J.P. Heremans, Phys. Rev. B 80 (2009) p.233201.

[16] Zhang, Q. et al. High thermoelectric performance by resonant dopant indium in nanostructured SnTe. Proc. Natl. Acad. Sci. U. S. A. 110, 13261–13266 (2013).

[17] Heremans, J. P., Wiendlocha, B. Chamoire, A. M. Resonant levels in bulk thermoelectric semiconductors. Energy Environ. Sci. 5, 5510–5530 (2012).

[18] Asheghi, M. and Kurabayashi, Katsuo and Kasnavi, R. and Goodson, Kenneth.Thermal conduction in doped single-crystal silicon films.Journal of Applied Physics 91,5079-5088 (2002)

[19] Huang, Rong Gao, Jie Wang, Xiaoyang.Extraordinary thermoelectric performance in MgAgSb alloy with ultralow thermal conductivity. Nano Energy (2019)

[20] Hobbis, D. et al. Structural, Chemical, Electrical, and Thermal Properties of n-Type NbFeSb. Inorg. Chem. 58, 1826–1833 (2019).